



# Enhancing mine groundwater system prediction: Full-process simulation of mining-induced spatio-temporal variations in hydraulic conductivities via modularized modeling



Shihao Meng<sup>a,b,c</sup>, Qiang Wu<sup>a,b,c,\*</sup>, Yifan Zeng<sup>a,b,c,\*</sup>, Leiyu Gu<sup>d</sup>

<sup>a</sup> National Engineering Research Center of Coal Mine Water Hazard Controlling, China University of Mining and Technology-Beijing, Beijing 100083, China

<sup>b</sup> National Mine Safety Administration Key Laboratory of Mine Water Hazard Controlling, Beijing 100083, China

<sup>c</sup> University of Mining and Technology (Beijing) Inner Mongolia Research Institute, Inner Mongolia 017000, China

<sup>d</sup> China Huaneng Coal Technology Research Co., Ltd, Beijing 100031, China

## ARTICLE INFO

### Article history:

Received 8 October 2024

Received in revised form 16 November 2024

Accepted 26 November 2024

Available online 14 December 2024

### Keywords:

Time-dependent permeability  
Overburden damage

Mine water inflow

Fluid-mechanical interaction  
Modular simulation

## ABSTRACT

The intricate interplay between rock mechanics and fracture-induced fluid flow during resource extraction exerts profound effects on groundwater systems, posing a pivotal challenge for promoting green and safe development in underground engineering. To address this, a novel numerical model with an explicit coupling simulation strategy is presented. This model integrates distinct modules for individual physical mechanisms, ensuring second-order accuracy through shared time integration, thereby overcoming limitations in simulating mining-induced strata damage, water flow, and permeability dynamics. A novel mathematical model is incorporated into the mechanical simulation to characterize the abrupt increase in permeability resulting from rock fracture propagation. This increase is quantified by evaluating the plastic damage state of rocks and incorporating a damage coefficient that is intrinsically linked to rock strength. The mechanical model tracks permeability changes due to mining. The flow model simulates aquifer-mine water interactions by calculating hydraulic conductivity and using dynamic zoning, adapting to mining progress. When applied to a case study of a complex mine, this approach significantly improved the accuracy of water inflow rate predictions by 57%.

© 2024 Published by Elsevier B.V. on behalf of China University of Mining & Technology. This is an open access article under the CC BY-NC-ND license (<http://creativecommons.org/licenses/by-nc-nd/4.0/>).

## 1. Introduction

The impact of large-scale human engineering activities on the environment and their underlying disaster-inducing mechanisms have emerged as a critical global issue [1,2]. In the realm of underground engineering, the inherent high in-situ stress field characteristics of subsurface rock masses necessitate that excavation-induced dynamic loads instantaneously release geostresses. Under the persistent static load from overlying strata, stress within the rock mass continuously adjusts until a new equilibrium state is achieved. Throughout this process, the superimposed effect of dynamic and static loads readily triggers the propagation and coalescence of fractures within the rock mass, ultimately leading to its damage. Notably, the evolution of the fracture field within the rock mass is not only directly related to the macroscopic damage process of the rock mass but also profoundly influences the dynamics of the seepage field [3,4].

Taking the Jurassic coalfields in western China as an example, this region accounts for 81.3% of the country's total coal production [5]. In this area, a single mining operation can extract coal seams with a thickness of up to 10 m, while the influence zone on the overlying strata extends to a remarkable depth of 300 m [6]. While high-intensity coal mining significantly enhances extraction efficiency, it also exacerbates disturbances to the overburden structure and groundwater system. As depicted in Fig. 1, with the progression of excavation, fractures within the overburden roof gradually initiate, propagate, and eventually coalesce, filling with water and facilitating seepage. This extensive and intense disturbance triggers a rapid influx of groundwater from the aquifer in the roof strata into the mine through the newly formed water-conducting fractures. These fractures, intimately connected to the mine, constitute stable drainage pathways within the groundwater system, thereby becoming decisive factors driving its dynamic evolution. In some mines, water inflows can reach astonishing rates of up to 8000 m<sup>3</sup>/h [7]. Such massive water volumes pose a severe threat to mine production safety and simultaneously challenge the regional ecological environment [8]. Beyond the extensive

\* Corresponding authors.

E-mail addresses: [wuq@cumtb.edu.cn](mailto:wuq@cumtb.edu.cn) (Q. Wu), [zengyf@cumtb.edu.cn](mailto:zengyf@cumtb.edu.cn) (Y. Zeng).

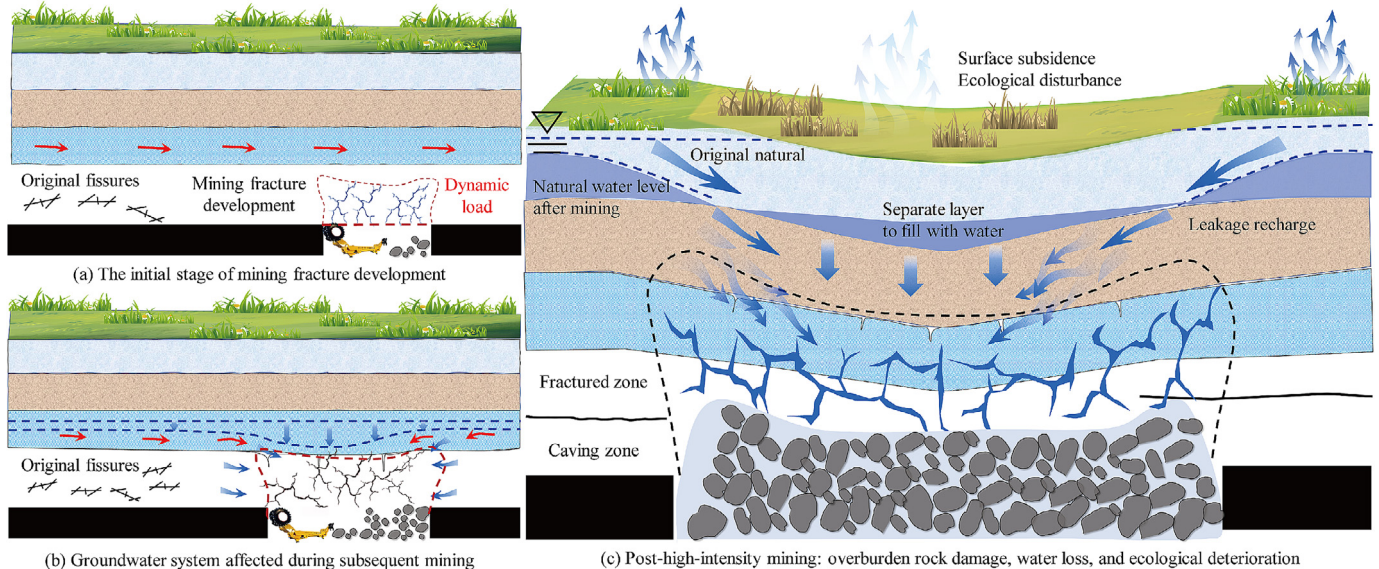


**Fig. 1.** Schematic diagram of the whole process of development, expansion, penetration, water filling and local healing of mining overburden fractures.

impacts on aquifer structures from high-intensity mining activities, the destruction of aquifer structures further alters water circulation processes on a broader scale [9]. Consequently, accurately depicting the topological changes of fracture networks within the overburden during mining activities and quantitatively simulating the nonlinear distribution of pore water pressure and dynamic variations in water volume within these fractures have emerged as critical challenges for achieving high-quality development in large-scale underground engineering projects.

With the continuous development of the underground engineering field, there has been a gradual deepening of understanding regarding the interaction between stress and seepage during excavation processes. Numerous scholars, both domestic and international, such as Biot, Terzaghi, Lu, and Zhang have conducted extensive and in-depth research on this topic, yielding substantial achievements [10]. In the exploration of coupled calculation methods, two primary approaches have emerged: the loosely coupled method and the directly coupled method. The loosely coupled method, also known as the iterative coupling method, involves separately calculating the seepage and stress field, and then coupling them through shared param. This method emphasizes mutual validation of results during the calculation process and solves problems based on convergence criteria. Studies by Vora et al. [11] demonstrate the practical application of this method. In contrast, the directly coupled method provides a more intimate analytical framework for the interaction between the flow field and rock deformation. In this approach, the seepage equation and stress-strain equation are directly solved simultaneously, fully considering the mutual influence between the two fields [12]. Although the directly coupled method exhibits higher accuracy in describing fluid-solid coupling processes, its solution difficulty increases significantly with the expansion of the simulation scope. To gain a more intuitive understanding of these complex underground processes, scholars have widely employed simulation software such as FLAC, PFC, COMSOL, and RFPA2D to conduct simulation analyses of underground activities like tunnel excavation and mining [13]. These studies have revealed the formation mechanism of seepage channels during excavation, but prediction and evaluation of water volume remain insufficient. In the field of groundwater modeling, the MODFLOW model, with its modular structure and ease of extension, has become the most widely used

standard model. MODFLOW and its related programs can not only simulate the interaction between groundwater and surface water (GSFLOW [14]) but also track particle movement trajectories (MODPATH [15]), model solute transport (MT3DMS [16]), describe groundwater flow with variable density and in unsaturated zones (SEAWAT [17]), and even simulate complex processes such as land subsidence (SUB [18]).

Currently, coal mining simulation research is confronted with two significant challenges pertaining to mechanics and flow field modeling. Firstly, the intense and sustained disturbance of coal mining activities on the overlying strata leads to pronounced changes in the mechanical properties and permeability of the rock strata [19]. These variations become increasingly evident as the degree of rock mass damage intensifies, posing a critical factor that must be addressed in the mechanics simulation process. Secondly, although Wu et al. [20] have clearly pointed out the practical application value of groundwater numerical simulation in mine water prevention and control research, precise simulation of the complex process of fracture seepage remains challenging in practical applications, falling short of meeting the in-depth requirements for regional water cycle evolution studies. In mine hydrogeological models, the drainage channels formed by the destruction of aquifer structures due to mining activities have emerged as the primary driving force for groundwater flow. This differs significantly from traditional hydrological models, where meteorological conditions or artificial pumping are primarily considered as driving forces [21]. Since traditional flow models do not encompass changes in structural param, their application scope and effectiveness are greatly limited when addressing mine groundwater issues. A coal mine can last for decades, and there is currently no model that enables both efficient calculations in engineering-scale simulations and correctly predicts the dynamic inflow under a wide range of coal mining disturbance conditions.

Therefore, effectively integrating mechanics simulation with flow simulation to precisely characterize the changes in the mechanical properties of rock strata and the complex process of fracture seepage during coal mining is an urgent issue in current coal mining simulation research. To address these challenges, this study innovatively proposes a simulation technology for the entire mining process. This technological framework encompasses three core components: mechanical damage simulation, flow field

driving simulation, and data exchange and inversion. Firstly, by constructing the stress-strain-fracture-permeability constitutive relationship of the mining-induced overlying strata, the spatio-temporal evolution characteristics of plastic strain and permeability param in the overlying strata are thoroughly analyzed, thereby determining the zoning and time-varying patterns of the caving zone, fracture zone, subsidence zone, and permeability coefficients in the mining-induced overlying strata. Secondly, based on the results of the mechanical damage simulation, the permeability zoning and time-varying patterns of the coal seam overlying strata are dynamically adjusted to drive the evolution of the groundwater system's flow field. In this process, the changes in water volume are accurately calculated based on the principle of mass conservation and the generalized finite difference simulation method. Through this comprehensive technical framework, it is expected to gain a deeper understanding of the mechanical and flow field changes during coal mining, providing more scientific and effective technical support for mine water prevention and control.

## 2. Methods

### 2.1. Technical framework for modular simulation

Mine groundwater simulation is a complex process that encompasses various physical mechanisms that are interdependent yet distinct in scale. Specifically, these mechanisms include: (1) damage to rock masses at the microscale; (2) the initiation, propagation, interconnection, and even partial closure of fractures caused by the destruction of overlying strata during mining; (3) the dynamic evolution of the entire groundwater system driven by the formation of these water-conductive fractures serving as drainage channels. To accurately simulate this entire process, it is imperative to appropriately handle the dynamic nature of the fracture network and the topological structure of the rock matrix over time. Existing analytical models typically adopt an implicit coupling approach by integrating these mechanisms into governing equations to accommodate their interactions. However, due to the high complexity of these interactions, it is often necessary to simplify and idealize certain mechanisms to a great extent. Notably, when dealing with the two processes of mining-induced overlying strata destruction and regional water cycle, the significant scale differences render traditional implicit coupling methods potentially insufficient.

To overcome this limitation, this study adopts a novel numerical model that employs an explicit coupling simulation strategy. Specifically, we have developed multiple individual modules to simulate these distinct physical mechanisms separately, with their interactions represented through data/information exchange between modules. The crux of this approach lies in the solid and fluid solvers sharing the same time integration method, ensuring that the overall error of the coupling method remains at the second-order level. Key modules in the numerical model include: (1) mechanical damage solver: for detailed depiction of the extent and degree of mining-induced overlying strata damage; (2) regional flow solver: generalizing the water cycle process driven by mining activities through the evolution of permeability param; (3) structural model: serving as the carrier for data exchange, encompassing the nonlinearity and hysteresis of interactions, particularly the time-varying nature of permeability. As illustrated in Fig. 2, within this numerical model, the fundamental function of the structural model is to receive rock deformation information from the mechanical solid solver, calculate stress responses and permeability changes, and provide this information to both the solid and fluid solvers. Within the same mining step, stress-strain responses are calculated through the mechanical module, and

permeability changes are derived. These changes in permeability param are then incorporated into the groundwater flow model to calculate groundwater level variations, which are fed back to the mechanical model to recalculate stress responses and permeability changes, iterating until convergence is achieved.

### 2.2. Mechanical module of mining disturbance

#### 2.2.1. Theoretical model

During the mining process, the damage mechanisms of the overlying strata and their accompanying fracture behaviors, particularly the shear dilation effect induced by shear deformation, the dynamic changes of fractures under reverse and cyclic loading, and their profound impacts on permeability properties, constitute a highly complex system. To accurately describe this system, it is of paramount importance to adopt mathematical models for simulation analysis. To better apply the evolution laws of rock damage and permeability to flow models at the engineering scale, this study has developed a two-stage, cross-scale mathematical model for seepage.

As illustrated in Fig. 3, the model takes into account the overall characteristics of fractured rock masses, which are composed of both rock matrix and fractures. The first stage focuses on the rock matrix scale (Fig. 3a), specifically addressing the sudden increase in permeability after the formation of fractures due to rock matrix damage, while neglecting the conventional stress-strain processes. This stage primarily concerns the changes in permeability before and after rock matrix damage. The second stage extends to the entire fractured rock mass scale (Fig. 3c), encompassing multiple groups of damaged rock matrices, where the properties of fractures dominate the entire seepage process.

The rationale of this model can be elaborated from both theoretical and practical engineering perspectives. From a theoretical standpoint, permeability variations are cross-scale phenomena that are challenging to directly capture through a single mechanical constitutive model. In contrast, from a practical engineering perspective, rocks overlying coal seams undergo a two-stage damage process: advanced stress damage due to initial mining activities and secondary damage during the mining process. The two-stage cross-scale model proposed in this study corresponds to these two stages: the first stage represents the consequences of advanced stress damage, while the second stage describes the secondary damage process dominated by variations in fracture aperture.

The process of permeability changes in the first stage can be clearly determined through comprehensive experiments on the full stress/strain-permeability relationship of rocks [22]. Before the rock reaches its peak strength (OB in Supplementary material Fig. 1), the existing microfractures and pores in the rock undergo a compaction process, accompanied by the generation and propagation of new microfractures. Although this process involves fine adjustments to the fracture network, the overall change in permeability remains relatively limited, exhibiting minor fluctuations. However, once the rock's plastic damage reaches a certain degree, typically near its peak strength, the permeability undergoes a drastic change, manifesting as a sudden increase that spans multiple orders of magnitude. This is due to the rapid formation of a connected macroscopic fracture network within the rock, significantly increasing the fluid flow pathways and thus leading to a substantial rise in permeability (Fig. 3b).

It is noteworthy that, in actual coal mining operations, due to abrupt changes in the stress field, the overlying strata often rapidly enter the plastic damage stage, resulting in an extremely short duration of the OB stage, where permeability changes can be deemed negligible compared to subsequent stages.

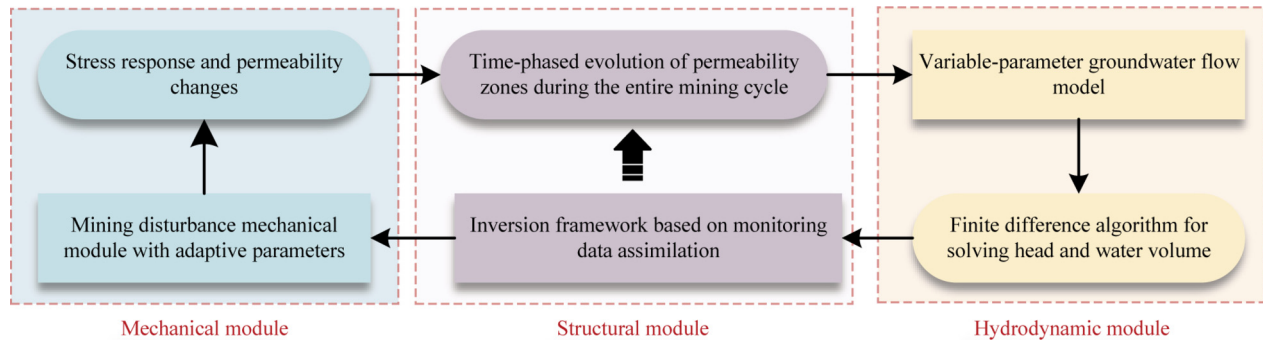


Fig. 2. Simulation technology framework.

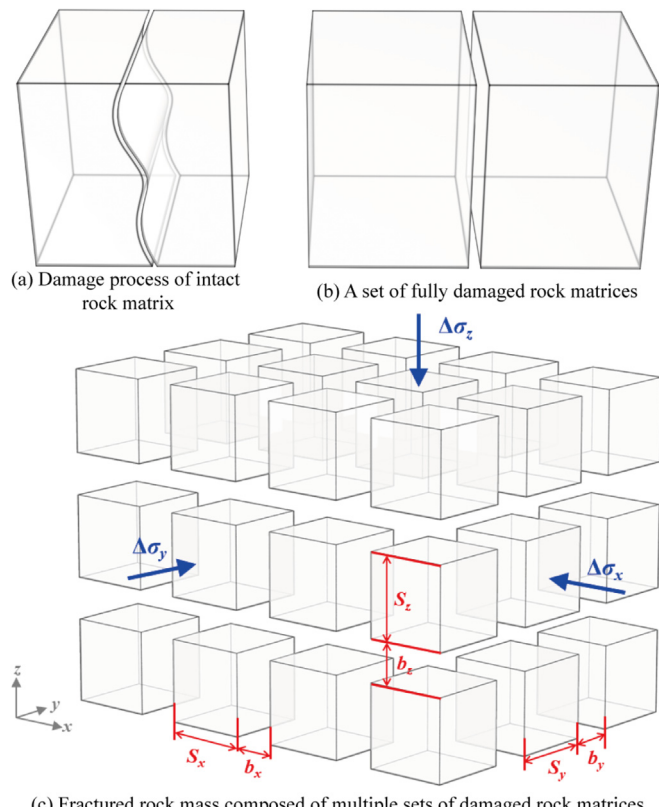


Fig. 3. Two-stage cross-scale seepage modelling.

Assuming stable permeability before the rock reaches its peak strength simplifies stage OB. The abrupt permeability increase stage, the rock fractures under loads exceeding its peak strength, with the sharp rise in permeability becoming the central focus of the model. As this phenomenon encompasses intricate physical mechanisms that are challenging to fully elaborate through purely theoretical derivations, the concept of a damage coefficient,  $\alpha$ , is introduced to quantitatively describe the nonlinear growth of permeability during rock damage. The  $\alpha$  is an empirical parameter based on experimental data, typically ranging from 1 to 3. Its value is related to the inherent properties of the rock, which is experimentally validated in Section 4.1. The incorporation of the  $\alpha$  enables the quantification of this complex process and allows the model to be flexibly adjusted based on different rock types and experiments. Taking the above into consideration, Eq. (1) establishes the first mathematical model for the permeability evolution of sandstone:

$$K_1 = K_0 \times 10^\alpha \quad (1)$$

where  $K_1$  is the permeability coefficient of the fractured rock mass during stage 1, L/T;  $K_0$  the permeability coefficient of the undamaged sandstone, L/T; and  $\alpha$  the damage coefficient, a function related to the properties of the rock, positively correlated with the rock strength.

In the second stage of rock mass seepage, also known as the fracture-dominated stage, the research shifts its focus to the intricate interplay between stress, strain, fracture aperture, and permeability, which forms the cornerstone of the second constitutive model. Compared to the abrupt increase stage, the changes in permeability during this stage, while still significant, no longer represent a leap in orders of magnitude but rather a smoother adjustment with the changes in fracture aperture. This model is grounded in the cubic law of single-fracture permeability, a fundamental principle that serves as the bedrock for analyzing fracture permeability characteristics. For sedimentary rocks, a typical layered rock mass, geological evidence indicates that they are often intersected by multiple sets of parallel, uniformly distributed, and equally spaced fracture networks [23]. The conceptual model of fractured rock mass, as depicted in Fig. 3c, comprises fractures and rock matrix. Studies have shown that although fractures in rock masses are minute, they serve as the primary conduit for groundwater flow after the damage of overburden strata, exhibiting permeabilities several orders of magnitude higher than pores [24]. Assuming that groundwater solely percolates through the fracture medium within the overburden strata, the entire overburden seepage medium can be regarded as an equivalent fracture network. Based on this understanding, Eq. (2)—the Louis formula—is employed to describe the overall permeability of a set of parallel fracture arrays:

$$K_2 = \frac{\rho g b^2}{12\mu} \cdot \frac{b}{s} \quad (2)$$

where  $b$  is the fracture aperture, L;  $s$  the average spacing between fractures, L;  $\rho$  the density of the fluid, ML<sup>-3</sup>; and  $\mu$  the dynamic viscosity coefficient of the fluid, ML<sup>-1</sup> T<sup>-1</sup>.

As external stress varies, the fracture aperture undergoes dynamic adjustments, leading to significant changes in the permeability coefficient. This relationship is precisely captured in Eq. (3), which reveals the nonlinear dependency between the permeability coefficient and the variation in fracture aperture, emphasizing that even minor changes in fracture aperture can have a substantial impact on permeability.

$$K_2 = K_1(1 - \Delta\mu_f/b)^3 \quad (3)$$

where  $\Delta\mu_f$  is the change in fracture aperture (with positive values indicating compressive displacement), L; and  $K_2$  the altered permeability coefficient of the fractured rock mass, L/T.

To comprehensively capture the behavior of this complex system, it is assumed that the total deformation of the fractured rock mass is comprised of both fracture deformation and deformation of the intact rock matrix, and under local stress equilibrium, the triaxial stress increments borne by the three components (intact rock matrix, fractures, and fractured rock mass) remain consistent. According to Hooke's law, in a three-dimensional orthogonal fracture medium, the permeability change in one direction is influenced by the strain variations induced by external actions (such as mining) in the other two orthogonal directions. At this point, the permeability of fractures is correlated with the three normal strains. When the strains can be reasonably distributed between the rock mass and fractures, changes in aquifer permeability can be estimated. Based on these assumptions and theoretical frameworks, Eq. (4) constructs the second constitutive model for the permeability evolution of sandstone [25]:

$$K_{2k} = \frac{1}{2} K_{1k} [(1 - \beta_i \Delta \varepsilon_i)^3 + (1 - \beta_j \Delta \varepsilon_j)^3] \quad (4)$$

where  $K_{2k}$  and  $K_{1k}$  are the permeability coefficients along direction  $k$  at stage 1 and 2, respectively,  $L/T$ ;  $k = z, x, y$ ;  $i = x, y, z$ ;  $j = y, z, x$ ;  $\beta$  the parameter related to the fracture density in a certain direction (the ratio of fracture aperture  $\sum b_k$  to the length of the fractured rock mass  $\sum S_k$ ) and the modulus reduction factor (the ratio of the elastic moduli of the intact rock matrix to the fractured rock mass); and  $\Delta \varepsilon$  the strain increment.

### 2.2.2. Sharp increase in permeability test for rock damage

To meticulously examine the pronounced surge in permeability subsequent to rock samples attaining peak strength, a series of rigorous and methodical experimental protocols were executed. The study initiated with the procurement of representative cores from the field using specialized drilling tools, which were subsequently processed into standardized specimens (50 mm × 100 mm) (Fig. 4a). Utilizing an advanced microcomputer-controlled servo triaxial seepage testing apparatus (Fig. 4e), permeability coefficient tests were conducted on the intact specimens (Fig. 4b) to establish baseline permeability data.

Upon completion of intact specimen testing, the versatility of the testing machine was harnessed to bisect the specimens using a Brazilian splitting mold. This enabled the investigation of permeability under fracture conditions, facilitated by the insertion of 0.01 mm shims (Fig. 4c). The machine's precision and stability ensured accurate measurement and recording of seepage flow data across varying fracture apertures, while maintaining consistent confining and osmotic pressures (Fig. 4d). These data facilitated the computation of corresponding permeability coefficients, enabling a profound analysis of the mechanisms responsible for the abrupt permeability enhancement post-stage 1.

Considering the actual burial depth range of the core, approximately 100 to 250 m, the experiment simulated its in-situ stress environment and rigorously controlled key variables. A confining pressure of 2.0 MPa was uniformly set to replicate the pressure conditions experienced by underground rocks, while the axial pressure was adjusted to 1.5 kN to maintain the stability of the test samples. Given the potential formation of a depression cone effect after coal mining, resulting in a maximum head difference of approximately 50 m, a permeation pressure difference of 0.5 MPa was set in the experiment to mimic the pressure gradient during actual seepage processes. By precisely measuring the seepage velocity and total flow rate, the permeability coefficient of the rock was calculated using relevant formulas. During the Brazilian splitting test, to ensure that the rock samples split cleanly along the predetermined direction, the loading rate was precisely controlled at 0.06 mm/min, which not only guaranteed the continuity of the test but also prevented non-uniform damage. By recording the

maximum axial pressure value at which the rock sample failed, the tensile strength of the rock could be accurately calculated, which is a crucial indicator for assessing the mechanical properties of rock materials.

### 2.2.3. Mechanical numerical simulation process

To better reflect the development process of overburden damage, this study employed a step-by-step mining approach in Itasca to simulate the underground mining process. For each mining step, the deformation and damage degree of the rock mass were dynamically evaluated, enabling parameter adaptation and dynamic zoning of the disturbed rock mass. This paper presents a dynamic adaptive parameter simulation algorithm during the mining process, as shown in Fig. 5, which mainly consists of four steps: mining, invoking the dynamic adaptive parameter module, fluid–solid calculation, and completing the mining. In the dynamic adaptive parameter module for mining-induced damage, all grid elements are traversed to determine their stress–strain states. If an element has not reached its peak strength (i.e., no plastic damage has occurred), it is classified as a normal element, and whether it belongs to the bending zone is determined based on its location, inherent properties, and strain degree. If an element undergoes plastic damage, it is adjusted to the first constitutive model mentioned above, and corresponding param are adjusted through the second constitutive model based on the current stress–strain state of the element, designating it as the fracture zone. When the element further reaches its residual strength after peak, it is adjusted to the strain-softening model, with corresponding param modified accordingly, and designated as the caving zone.

The Itasca numerical modeling code harnesses explicit solutions of Newton's laws of motion as its computational backbone, with these solutions being modular and adaptable for integrations like implicit heat transfer and dynamic multi-step computations. The model evolves through iterative time steps, each containing a pre-defined sequence of operations. For fluid flow or coupled flow simulations using FLAC3D, estimating the time scales of involved processes is crucial [26]. Knowing these time scales and diffusivity helps determine critical parameters such as grid dimensions, zone sizes, time step magnitudes, and overall feasibility.

Characteristic time scales can be conceptualized using definitions from dimensional analysis, providing a foundation for approximating time scales relevant to FLAC3D analyses. Characteristic time of the mechanical process ( $t_c^m$ ) and the diffusion process ( $t_c^f$ ) in the Eq. (5).

$$t_c^m = \sqrt{\frac{\rho}{K_u + 4/3G}} L_c \quad (5)$$

$$t_c^f = \frac{L_c^2}{c} \quad (5)$$

where  $K_u$  is the undrained bulk modulus,  $ML^{-1}T^{-2}$ ;  $G$  the shear modulus,  $ML^{-1}T^{-2}$ ;  $L_c$  the characteristic length,  $L$ , interpreted as the average length of the flow path traversing the medium; and  $c$  the diffusivity related to permeability,  $L/T$ .

The Cauchy motion equation for a grid element within a continuous medium can be expressed by Eq. (6).

$$\sigma_{ijj} + \rho \mathbf{b}_j = \rho \frac{d\mathbf{v}_i}{dt} \quad (6)$$

where  $\sigma_{ijj}$  is the stress tensor on the element;  $\mathbf{b}$  the body force vector acting on the element; and  $\frac{d\mathbf{v}_i}{dt}$  the acceleration vector of the medium.

The constitutive relationship is defined by Eq. (7).

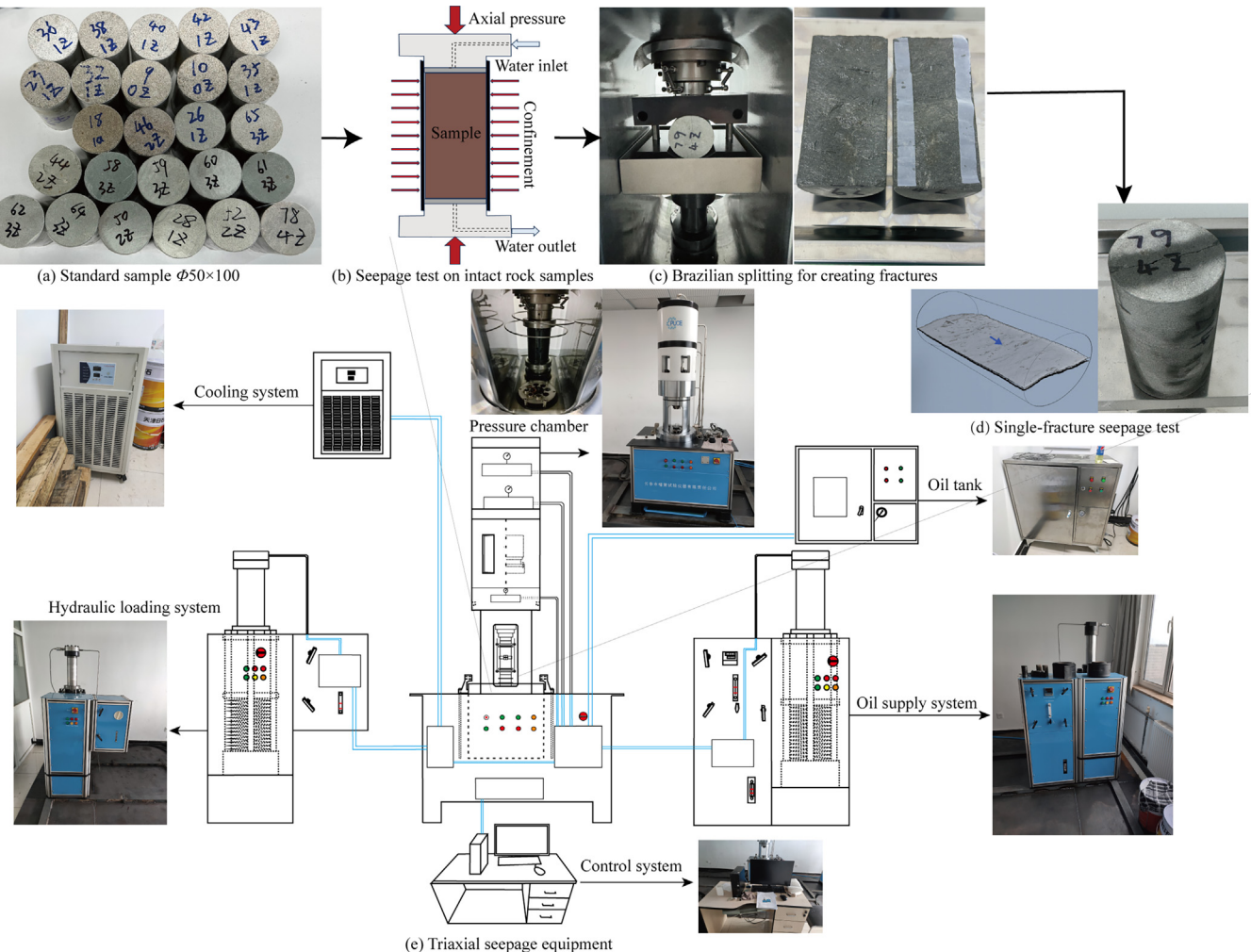


**Fig. 4.** Experimental equipment and procedures for seepage experiments on intact rock and single-fracture rock.

$$[\dot{\sigma}]_{ij} = F_{ij}(\sigma_{ij}, \xi_{ij}, \kappa) \quad (7)$$

where  $[\dot{\sigma}]_{ij}$  is the co-rotational stress-rate tensor;  $F_{ij}$  the tensor function, related to both the stress tensor and the strain tensor;  $\sigma_{ij}$  the stress tensor;  $\xi_{ij}$  the strain tensor; and  $\kappa$  the parameter that accounts for the loading path.

Additionally, the constitutive relationships for these two materials warrant special attention. For null material, it signifies that the material has been removed or excavated from the model, and the stress within the null element is automatically set to zero. This can be utilized to simulate excavation processes underground. As for rock elements, the Mohr-Coulomb model is adopted, which effectively describes the elastoplastic deformation and damage characteristics of rocks under stress. The damage envelope of this model strictly follows the Mohr-Coulomb criterion.

### 2.3. Regional groundwater flow module

To overcome the limitation of current groundwater simulation technologies in fully representing the water inrush process throughout the entire mining-induced damage cycle, this study developed a data import interface using Fortran language to integrate the permeability evolution constitutive relationships obtained from the aforementioned mechanical models. Based on the dynamic adaptive parameter mining-induced damage module of the mechanical models in the previous research, the destructive

effects throughout the entire coal mining cycle were characterized, enabling the gradual destruction of aquifer structures and the gradual increase in permeability within the disturbed area as the coal mining face advances. By utilizing permeability parameter zoning based on dominant fracture sets and the macro-equivalent permeability coefficient generalized by the equivalent medium theory, the study investigated the permeability zoning and time-phased evolution of the disturbed area throughout the entire mining cycle. This integrated module was then embedded into the MODFLOW6 groundwater simulation [27], and the flow field was solved through an iterative finite difference algorithm, thereby achieving dynamic simulation of groundwater system changes driven by mining-induced dynamic damages.

In the process of optimizing regional water flow simulation, for the MODFLOW flow model, improvement strategies focus on gaining a deep understanding of its source code architecture, layout, and core functionalities. Based on this foundation, the research emphasizes refining and enhancing the dynamic simulation capabilities of water flow interactions between horizontal and vertical grids. The core improvement direction involves constructing an innovative program package, a module centered on establishing a dynamic mathematical relationship model between permeability param and coal seam mining progress. This model aims to precisely capture and quantify the real-time impacts of mining activities on the groundwater levels and permeability coefficients of disturbed coal seam units, ensuring that within each stress cycle of the simu-

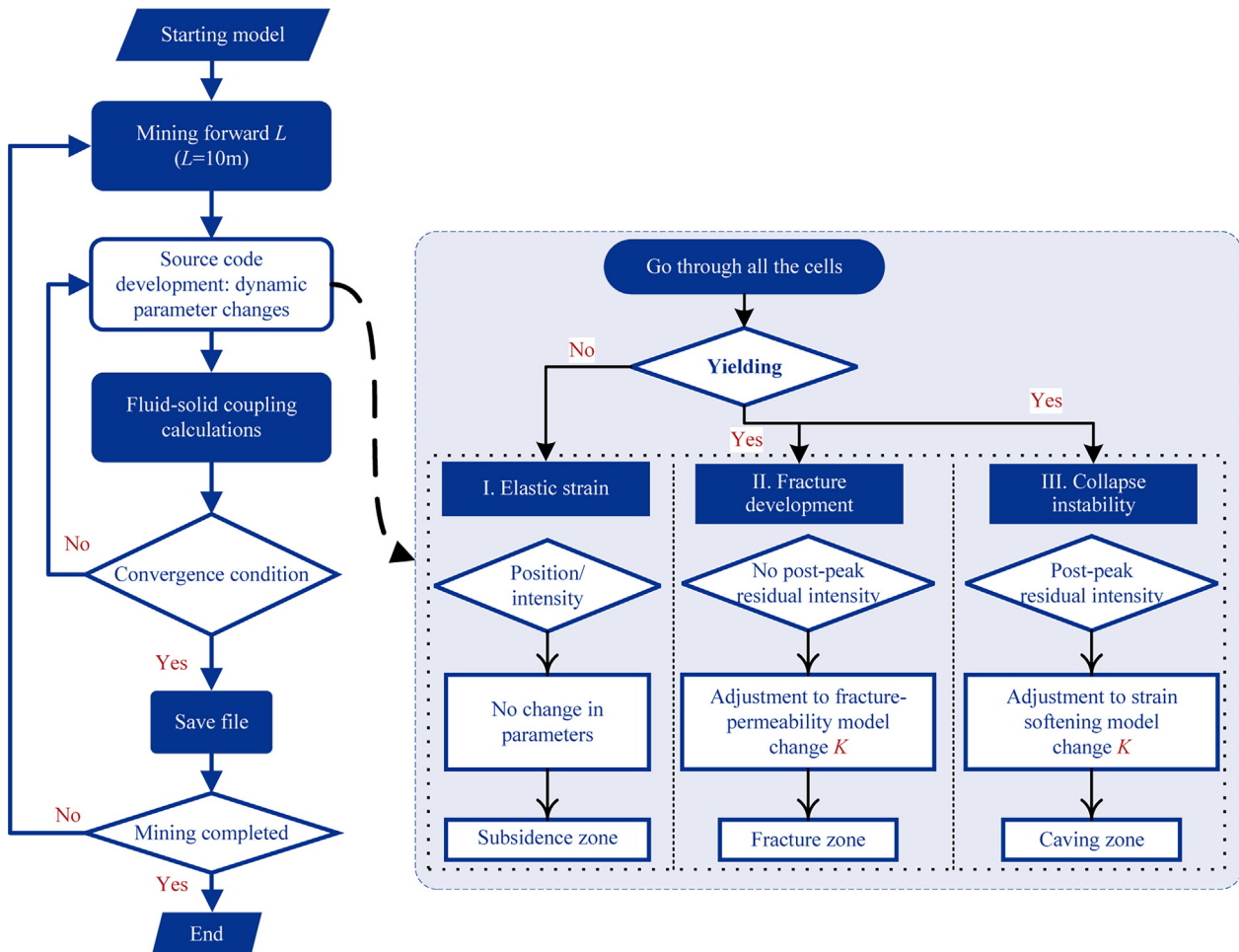


**Fig. 5.** Mining damage module based on dynamic adaptive param.

lation, the permeability coefficients in the affected areas can dynamically reflect the latest advancements of mining activities. This requires the model not only to accurately describe the spatial variability of permeability coefficients but also to achieve dynamic adjustments over time, comprehensively reflecting the complex impacts of mining activities on the groundwater flow field.

To implement this improvement plan, the first step is to conduct a thorough analysis of the source code of the Node Property Flow (NPF) package within MODFLOW6. Following this, a brand-new package will be developed and integrated, which incorporates the aforementioned dynamic mathematical model, enabling automatic and real-time adjustment and updating mechanisms for permeability coefficients. This process underscores the significance of technical collaboration and code compatibility testing to ensure seamless integration of the new module with the original system, while maintaining the stability and efficient operation of existing functionalities.

### 2.3.1. Theoretical model

The default assumption within the NPF package is that the principal axes of hydraulic conductivity align with the global model coordinate system of ( $x, y, z$ ). Consequently, the hydraulic conductivity tensor  $\mathbf{K}$  in this global coordinate system is represented by a diagonal matrix (Eq. (8)).

$$\mathbf{K} = \begin{pmatrix} K_{xx} & 0 & 0 \\ 0 & K_{yy} & 0 \\ 0 & 0 & K_{zz} \end{pmatrix} \quad (8)$$

where  $K_{xx}$ ,  $K_{yy}$ , and  $K_{zz}$  are values of hydraulic conductivity, L/T along the  $x$ ,  $y$ , and  $z$  coordinate axes.

In MODFLOW 6, the discrete control volumes are referred to as model "cells". Within each cell, there exists a point known as a "node", where the head is calculated. The hydraulic connectivity between cells is conceptualized as conductive connections between these nodes, mimicking the natural flow paths of groundwater through the subsurface. The combined assembly of model cells and their associated network of connections is collectively termed the model "grid". The flow between cells is defined as "internal flow", which is mathematically described through the discretized form of Darcy's law. Specifically, the water flux between two adjacent cells can be precisely expressed as the product of the hydraulic conductance between these cells and the head difference across them. This representation is known as the "conductance-based" flow formulation [27]. Precisely, the horizontal flow from cell  $m$  to cell  $n$  is given by Darcy's law (Eq. (9)):

$$Q_{n,m} = \bar{K}_{n,m} \Delta w_{n,m} \Delta v_{n,m} \frac{h_m - h_n}{L_{n,m} + L_{m,n}} \quad (9)$$

where  $Q_{n,m}$  is the flow volume entering cell  $n$  from cell  $m$ ,  $L^3$ ;  $\bar{K}_{n,m}$  the effective hydraulic conductivity between these two nodes,  $L/T$ ;  $\Delta w_{n,m} \Delta v_{n,m}$  the flow traverses a cross-sectional area,  $L^2$ , where  $\Delta v_{n,m}$  the height of the face through which flow occurs,  $L$ , related to the saturated thickness of the cell; the water heads at nodes  $m$  and  $n$  denoted by  $h_m$  and  $h_n$ , respectively,  $L$ ; and  $L_{n,m}$  the distance from the center of cell  $n$  to the shared face with cell  $m$ ,  $L$ .

The conductance,  $C_{n,m}$ , is a parameter that encapsulates all factors except the head terms (Eq. (10)). It represents a combination of information related to the hydraulic conductivity and the dimensions of the two adjacent cells. This conductance parameter will be repeatedly referenced in subsequent calculations, as it plays a pivotal role in determining the flow between cells in groundwater models. By pre-computing  $C_{n,m}$  for each pair of adjacent cells, the model simplifies the flow calculation process by allowing the direct use of the head difference between cells to determine the flow volume, modulated by the previously established conductance [27].

$$C_{n,m} = \frac{\bar{K}_{n,m} \Delta w_{n,m} \Delta v_{n,m}}{L_{n,m} + L_{m,n}} \quad (10)$$

In the case of confined layers, a constant saturated thickness is maintained during the simulation process, meaning their groundwater levels are always above the elevation of the aquifer roof. The transmissivity ( $T$ ) of confined layers is calculated by multiplying the hydraulic conductivity by the unit saturated thickness ( $\Delta v$ ), where for confined layers,  $\Delta v$  is equivalent to the unit thickness. Eq. (11) is utilized within Modflow to compute this using the unit elevation data from the discretization file.

$$\Delta v_n = S_{F_n} (\text{TOP}_n - \text{BOT}_n) \quad (11)$$

where  $\text{TOP}_n$  and  $\text{BOT}_n$  are the elevation of the top/bottom of the cell  $n$ ,  $L$ ; and  $S_{F_n}$  the saturated fraction [28].

Assuming a uniform transmissivity within a single cell, which is the product of hydraulic conductivity and thickness, there can be discrete changes in transmissivity at the boundaries between any two cells. Consequently, the conductance between nodes is analogous to the equivalent conductance of two series-connected half-cells. This equivalent conductance can be calculated using the “harmonic mean” method (Eq. (12)) outlined by McDonald and Harbaugh [29].

$$C_{n,m} = \left( \frac{L_{n,m} + L_{m,n}}{\frac{L_{n,m}}{T_{n,m}} + \frac{L_{m,n}}{T_{m,n}}} \right) \frac{\Delta w_{n,m}}{L_{n,m} + L_{m,n}} \quad (12)$$

where  $T_{m,n} = \Delta v_m K_{m,n}$  is the transmissivity,  $L^2/T$ ; and  $K_{m,n}$  the hydraulic conductivity of cell  $m$  in the direction of cell  $n$ .

In the simulation of confined and convertible layers, Eq. (13) is utilized to calculate the vertical hydraulic conductivity, a crucial parameter for assessing the characteristics of vertical groundwater flow. To ensure computational accuracy, each cell must possess information on vertical hydraulic conductivity. This information can be obtained by directly specifying the vertical hydraulic conductivity as input data or indirectly calculated by inputting the ratio of horizontal to vertical hydraulic conductivities. For convertible layers, since their saturated thickness varies with changes in water head during the simulation process, the vertical hydraulic conductivity needs to be recalculated in each iteration to reflect the current hydrogeological conditions.

$$\frac{1}{C_{n,m}} = \frac{1}{\frac{A_{n,m} K_{n,m}}{(1/2)\Delta v_{n,m}}} + \frac{1}{\frac{A_{n,m} K_{m,n}}{(1/2)\Delta v_{m,n}}} \quad (13)$$

where  $A_{n,m}$  is the flow area of the connection (as viewed from above) between cells  $n$  and  $m$ ,  $L^2$ .

### 2.3.2. Coal mining disturbance (CMD) new package

Based on a thorough analysis of the source code program, it is essential to clarify that since constant param in the Allocate and Read (AR) package are read outside the stress period loop, the new program package necessitates re-reading permeability param within the stress period loop and updating them in real-time

according to the stress period. This design ensures that each stress period reflects the latest geological and hydrological condition changes. Additionally, once the permeability param of each grid cell are read, they are immediately used in subsequent calculation processes, which involve calculating horizontal and vertical equivalent transmissivities based on the contact relationships between grids and saturated thicknesses. Throughout the simulation process, the permeability param invoked in subsequent calculations are these calculated equivalent transmissivities.

Furthermore, the application of mechanical models enables precise tracking of the disturbance range caused by coal mining activities on the overlying strata within each stress period. However, mapping this disturbance range onto the grid cells in the flow model and identifying the disturbed areas during specific stress periods in the flow simulation poses a technical challenge. To address this issue, the concept of permeability coefficient zoning layers is introduced, where undisturbed areas maintain normal parameter assignments, while disturbed areas are specially identified by assigning permeability coefficients significantly larger than normal values (e.g., values greater than 10). After reading these param, the program package uses logical judgments. If the permeability coefficient exceeds a set threshold, the INT function combined with dividing the permeability coefficient by 10 is utilized to automatically extract a unique identifier representing the disturbed stress period. This mechanism not only achieves precise delineation of disturbed areas but also facilitates dynamic adjustment and evolution of permeability param.

In summary, the program package has undergone significant functional expansions (Fig. 6), primarily in two aspects: (1) It implements a dynamic reading and change processing mechanism for param within stress periods, encompassing real-time reading of permeability coefficients, automatic identification and marking of disturbed areas, restoration of initial permeability coefficients, adjustment of permeability coefficients in disturbed areas based on stress period changes, and calculation of equivalent transmissivities based on interactions between cells and changes in saturation states. (2) It optimizes the results output, adding a precise calculation module for mine water inflows and enriching the output content of new param, thereby comprehensively enhancing the simulation's accuracy and practicality.

## 3. Synthetic example

### 3.1. Hydrogeological characteristics

The Caojitan coal mine, situated in the core of Phase I planning in the Yushen mining area of northern Shaanxi, China (in the [Supplementary material Fig. 2a](#)), operates amidst arid conditions with seasonal rainfall concentrated in July to September. Its extensive well field, spanning 108.49 km<sup>2</sup> (in the [Supplementary material Fig. 2b](#)), harbors vast coal reserves of 1.511 billion tonnes, supporting an annual output of 25 million tonnes. Despite a simple geological structure conducive to mining, the region faces environmental sensitivity.

The mine's 2–2 coal seam is strategically segmented into east and west panels, with groundwater categorized into three aquifers and a confining layer (in the [Supplementary material Fig. 2d](#)). Analysis along the mining face's profile line A-A' reveals distinct aquifer characteristics: a low-permeability “normal bedrock aquifer,” a highly permeable “weathered bedrock aquifer” directly recharged by mining fractures, and an ecologically vital “Quaternary aquifer” separated by a variable-thickness Neogene red clay confining layer. Notably, the western section lacks this clay barrier.

Field data analysis depicts evolving groundwater dynamics. From December 2021 to February 2022 (in the [Supplementary material Fig. 3](#)), two groundwater level funnels emerged in the

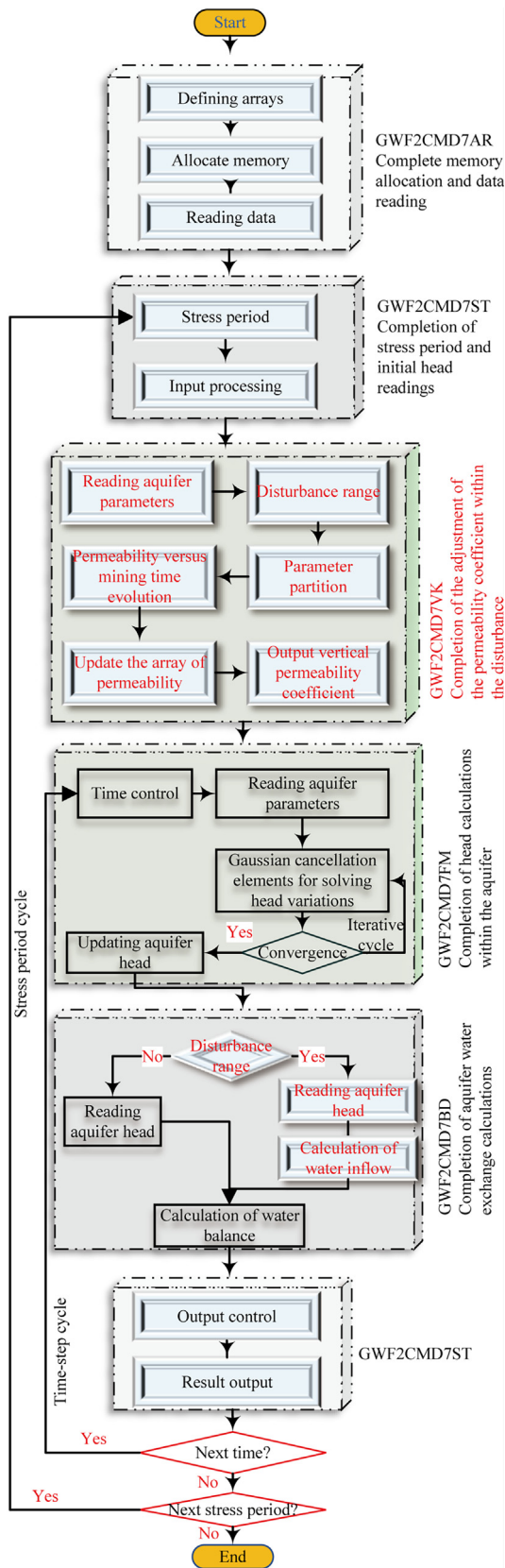


**Fig. 6.** Mine hydrogeological simulation program flow.

weathered bedrock aquifer, with one stabilizing and the other expanding its reach. The study area, characterized by minimal tectonic activity and flat geological layers, experiences mining-

induced fractures that facilitate groundwater ingress. Above the coal seam, three distinct zones—caving, fracture, and subsidence—manifest, with fracture zone heights varying from 134 to 183 m, measured through boreholes LD-1, LD-2, and LD-3, placed at different positions around the mining face (in the [Supplementary material Fig. 2c](#)). This disturbance pattern mimics a saddle shape, peaking near the weathered bedrock aquifer (in the [Supplementary material Fig. 4](#)).

The 16 cores used in the experiment were from the LD-3 borehole and were classified as weathered sandstone, fine sandstone, siltstone and argillaceous siltstone. The buried depth is distributed in 100–250 m. Its saturated water absorption and dry density are shown in the following [Table 1](#).

### 3.2. Mechanical model

In the process of numerical simulation, the scale of the model and the refinement of the mesh division both have significant impacts on the accuracy of the results. This study focuses on the mining process of the 122107 working face after the completion of mining in the 122109 working face. For this purpose, the 122107 working face is selected as the analysis object. As shown in the [Supplementary material Fig. s5](#), the model is set with a length of 600 m and a mining face advancement length of 300 m. Furthermore, considering the potential interference to the stress-strain analysis of the mining face caused by the proximity between the mining face edge and the fixed displacement boundary, the model width is set to 400 m.

In the numerical model, the stratigraphic layers are approximated as horizontally distributed. To enhance the accuracy of numerical simulation calculations, the actual stratigraphic lithology is grouped into a total of 27 layers. Additionally, the six lithological parameters required by the Mohr-Coulomb constitutive model—bulk modulus, shear modulus, tensile strength, internal friction angle, cohesion, and density—can all be obtained through indoor rock physico-mechanical testing. This is illustrated in the [Supplementary material Table s1](#).

### 3.3. Flow model

Based on the geological and hydrogeological context of the Caojiatan Coal Mine, the modeling framework is conceptually stratified into five vertical layers: Quaternary unconfined aquifer, Neogene Baode Formation clayey aquitard, weathered Anding Formation confined aquifer, Zhiluo and Yan'an Formations' bedrock confined aquifer, and the 2–2 coal seam. Vertically, the upper Quaternary aquifer interacts with atmospheric precipitation through infiltration and evaporation, using the phreatic surface as its upper water boundary. The coal seam floor at the bottom serves as a water-impermeable boundary. Horizontally, to minimize modeling errors from boundary assumptions, the mining field's right edge is treated as a third-type boundary for water exchange, while also functioning as a water-resisting barrier. Specifically, the Quaternary aquifer, weathered Anding aquifer, and peripheral Zhiluo-Yan'an bedrock aquifers are designated as third-type boundaries. Conversely, the Baode Formation clayey aquitard and 2–2 coal seam surroundings are water-resistant boundaries. The Quaternary aquifer's watershed is also considered water-resistant. A hydrogeological conceptual model is established, as illustrated in [Fig. 7](#), encompassing these layers and boundary conditions.

Based on the analysis of the aforementioned groundwater flow characteristics (in the [Supplementary material Fig. 4](#)), it can be observed that a stable funnel was formed in the weathered bedrock aquifer after the completion of mining in the 122109 working face. Therefore, this simulation selects the completion of mining in the 122109 working face as the initial moment, and utilizes the

**Table 1**

Classification and Basic Properties of Rock Samples.

ID	Color	Lithology	Depth (m)	Water absorption under saturated (%)	Dry density (g/cm <sup>3</sup> )
16-1a	Brownish red	Weathered sandstone	87.70	12.64	1.89
04-0z	Brownish green	Weathered sandstone	106.76	8.51	1.91
22-1a	Brownish green	Weathered sandstone	107.13	14.00	1.85
11-0z	Off-white	Fine sandstone	193.06	5.68	2.09
67-3z	Off-white	Fine sandstone	200.67	7.65	2.01
36-1z	Off-white	Fine sandstone	205.49	4.28	2.34
41-1z	Off-white	Fine sandstone	240.00	8.98	2.13
43-1z	Off-white	Fine sandstone	241.60	7.34	2.36
46-2z	Off-green	Siltstone	110.75	1.61	2.27
59-3z	Off-white	Siltstone	133.54	1.78	2.18
63-3z	Off-green	Siltstone	154.28	1.05	2.36
52-2z	Off-white	Argillaceous siltstone	189.76	3.25	2.13
81-4y	Off-white	Argillaceous siltstone	242.70	2.63	2.31

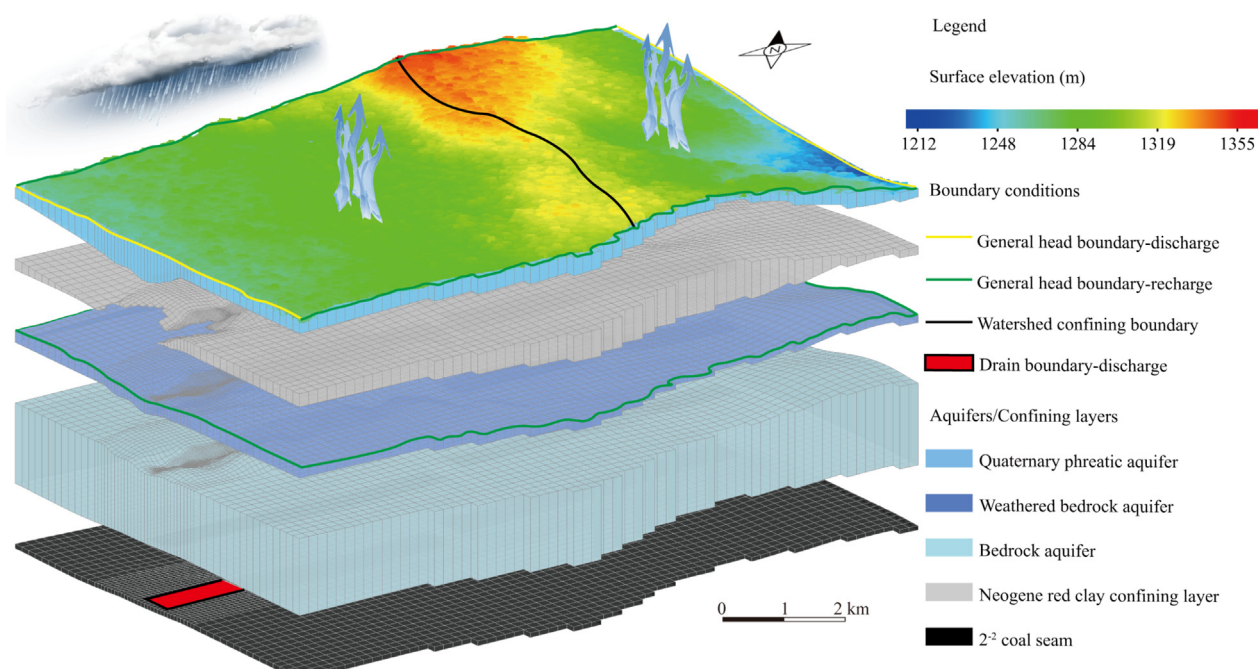
numerical model to determine the stable flow's head distribution, which serves as the initial head condition for subsequent simulations of mining in the 122107 working face.

Hence, this simulation first establishes a steady-flow model. By utilizing long-term observation well data of groundwater levels, regional flow fields, and measured water inrush volumes at the completion of mining in the 122109 working face, the boundary conditions and hydrogeological param are identified. The governing equations for steady-flow groundwater flow and boundary control are presented in Eq. (14). Based on the steady-flow model, the identified aquifer groundwater levels, hydrogeological param, and boundary conditions are used as initial conditions to conduct subsequent unsteady-flow numerical simulation experiments for mining in the 122107 working face. The governing equations for unsteady-flow groundwater flow and boundary control are presented in Eq. (15).

Due to safety and policy constraints, it is not feasible to set up groundwater level monitoring boreholes above the working face. Especially for bedrock aquifers, the impact of mining activities is

limited in scope, resulting in minimal changes in groundwater level monitoring data outside the working face. Consequently, the flow field interpolated from monitoring data fails to accurately reflect the post-mining flow field state. In such circumstances, utilizing steady-state flow simulations to optimize initial conditions becomes particularly crucial, especially in research areas where groundwater level data is scarce, as this method offers significant assistance. Furthermore, through steady-state flow simulations, model parameters can be further identified and optimized, thereby effectively enhancing the accuracy of the simulations.

$$\left\{ \begin{array}{l} \frac{\partial}{\partial x} (K_{xx} \frac{\partial h}{\partial x}) + \frac{\partial}{\partial y} (K_{yy} \frac{\partial h}{\partial y}) + \frac{\partial}{\partial z} (K_{zz} \frac{\partial h}{\partial z}) + \varepsilon = 0, x, y, z \in \Omega_1 \\ \frac{\partial}{\partial x} (K_{xx} (h - h_b) \frac{\partial h}{\partial x}) + \frac{\partial}{\partial y} (K_{yy} (h - h_b) \frac{\partial h}{\partial y}) + K_{zz} (\frac{\partial h}{\partial z})^2 + \varepsilon = 0, x, y, z \in \Omega_2 \\ h(x, y, z) = h_0, x, y, z \in \Omega \\ K \frac{\partial h}{\partial n} \Big|_{\Gamma_1} = q, x, y, z \in \Gamma_1 \\ K \frac{\partial h}{\partial n} \Big|_{\Gamma_2} = \frac{K}{m} (h_2 - h), x, y, z \in \Gamma_2 \end{array} \right. \quad (14)$$

**Fig. 7.** Conceptual model of hydrogeology.

$$\left\{ \begin{array}{l} \frac{\partial}{\partial x}(K_L \frac{\partial h}{\partial x}) + \frac{\partial}{\partial y}(K_L \frac{\partial h}{\partial y}) + \frac{\partial}{\partial z}(K_z \frac{\partial h}{\partial z}) + \varepsilon = S \frac{\partial h}{\partial t} x, y, z \in \Omega_1, t \geq 0 \\ \frac{\partial}{\partial x}(K_L(h - h_b) \frac{\partial h}{\partial x}) + \frac{\partial}{\partial y}(K_L(h - h_b) \frac{\partial h}{\partial y}) + K_z (\frac{\partial h}{\partial z})^2 + \varepsilon = \mu \frac{\partial h}{\partial t} x, y, z \in \Omega_2, t \geq 0 \\ h(x, y, z, t)|_{t=0} = h_1 x, y, z \in \Omega \\ K \frac{\partial h}{\partial n} \Big|_{\Gamma_1} = q x, y, z \in \Gamma_1, t \geq 0 \\ K \frac{\partial h}{\partial n} \Big|_{\Gamma_2} = \frac{K}{m'}(h_2 - h) x, y, z \in \Gamma_2, t \geq 0 \end{array} \right. \quad (15)$$

The aquifer system consists of a phreatic aquifer ( $\Omega_1$ ) and a confined aquifer ( $\Omega_2$ ), with groundwater level elevation denoted by  $h$ ,  $L$ .  $h_b$  is elevation of the phreatic aquifer's bottom,  $L$ ;  $\varepsilon$  the source/sink term of the aquifer,  $1/T$ ;  $S$  the specific storage coefficient of the aquifer,  $1/L$ ;  $\mu$  the specific yield of the phreatic aquifer;  $h_0, h_1$  the initial groundwater level values interpolated from observed and calculated by a steady-flow model, respectively,  $L$ ;  $K \frac{\partial h}{\partial n}$  the hydraulic conductivity normal to the boundary,  $L/T$ ; and  $\Gamma_1$  and  $\Gamma_2$  the flow boundary (second-type) and general head boundary (third-type), respectively. Where  $q$  is the given flow rate on the flow boundary,  $L^3/T$ ; and  $K$  and  $m'$  the hydraulic conductivity,  $L/T$ , and thickness of the aquifer,  $L$ , respectively, between the general head boundary and the location of the given head  $h_2$ .

The newly developed CMD package was utilized to simulate the coal mining process. Furthermore, instead of presetting an initial value for the water inrush volume in the gob, the gob was designated as a planar layer, and the Drain (DRN1) package (Eq. (16)) was employed for calculation. By continuously adjusting the model param, the calculated water inrush volume was aligned with the actual observed values. Additionally, incorporating long-term observation well groundwater level data enabled precise identification and validation of the model param.

$$Q_{out} = \begin{cases} CD(h_n - HD), h_n > HD \\ 0, h_n \leq HD \end{cases} \quad (16)$$

where  $Q_{out}$  is the discharge flow rate at the outlet,  $L^3 \cdot T^{-1}$ ;  $CD$  the conductivity of the drain,  $L^2 \cdot T^{-1}$ ;  $HD$  the elevation of the discharge outlet,  $L$ ; and  $h_n$  the head of the cell  $n$ ,  $L$ .

The monthly average rainfall and evaporation intensity at the limiting depth are presented in the [Supplementary material Fig. 6a](#) and [Table 2](#). Additionally, the parameter zones for rainfall infiltration coefficient and evaporation intensity were set according to land use type distribution with a 10 m resolution, as shown in the [Supplementary material Fig. 6b](#) and [Table 3](#). Within the study area, 174 boreholes were collected, with 37 containing hydrogeological data. Innovations were made in parameter zoning. Based on multi-source data fusion results, zoning for hydraulic conductivity and specific yield/storage coefficient was carried out, focusing on water-rich partitions. Initial parameter values were derived from regional empirical data. These values and zoning were then refined through simulation, identification, and verification. The final zoning is illustrated in the [Supplementary material Fig. 6c](#) and d, with detailed values provided in the [Supplementary material Tables 3 and 4](#).

## 4. Results

### 4.1. Comparison of seepage flow in fractures of different lithologies

Regarding the lithological classification of the strata above the first mining coal seam, Brazilian splitting tests and permeability measurements before and after the tests were conducted on corresponding core samples. The  $\alpha$  induced by splitting was calculated using Eq. (1), and the specific results are detailed in [Table 2](#). The

in-depth analysis revealed that the lithology of this strata can be clearly divided into three categories: weathered bedrock located at the top of the bedrock, poorly cemented fine-grained sandstone, and densely structured siltstone or argillaceous siltstone. The weathered bedrock is shallowly buried (approximately 100 m below the surface), has a loose structure, and generally exhibits a tensile strength below 2.0 MPa, accompanied by a relatively high permeability coefficient of up to  $10^{-5}$  cm/s. In contrast, the tensile strength of fine-grained sandstone increases with burial depth to approximately 2.5 MPa, reflecting the improved cementation degree with increased burial depth, while its permeability coefficient correspondingly decreases to  $10^{-6}$  cm/s. Dense sandstone exhibits a higher tensile strength (8.2 MPa) and an extremely low permeability coefficient ( $10^{-9}$  cm/s). Compared to pure siltstone, argillaceous siltstone exhibits slightly reduced strength.

A comparative analysis of the permeability changes before and after splitting for different lithological samples using logarithmic coordinates ([Fig. 8](#)) reveals that the permeability change of weathered bedrock after splitting is the most subtle. The permeability of fine-grained sandstone decreases with increasing burial depth, but the increase in permeability caused by splitting becomes gradually more significant. Although the initial permeability of dense sandstone is the lowest, its permeability increase after splitting is the most pronounced.

This series of analyses clearly indicates that the permeability of rocks and its changes after splitting are closely related to the strength characteristics of the rocks themselves. Dense rocks exhibit reduced permeability due to increased strength, while the fracture structure introduced by splitting significantly enhances permeability. In contrast, the additional improvement in permeability caused by splitting in loosely structured rocks with well-developed pore structures is relatively limited. To further quantify the relationship between rock strength and permeability, [Fig. 9a](#) and b respectively show the correlation between the tensile strength of rocks and the permeability of intact samples, as well as the mutation increase in permeability of split samples. The former relationship shows a pronounced negative nonlinear correlation between the permeability coefficient ( $K$ , cm/s) and the tensile strength ( $T$ , MPa), with a fitting expression of  $K=1.547 \times 10^{-4} T^{-4.674}$  and a high goodness-of-fit value of  $R^2=0.930$ . In contrast, the latter exhibits a positive linear correlation between the  $\alpha$  and  $T$ , with a fitting expression of  $\alpha=-0.282 + 0.317T$  and an  $R^2$  value of 0.899, indicating a good fit.

### 4.2. Time-dependent permeability

Exploring fracture development through numerical simulations focuses on the evolution of plastic zones, categorized into three types: single-shear, single-tensile, and combined shear-tensile. As mining commences, plastic deformation initiates in the coal seam's surrounding rock, with tensile damages emerging in the overburden, initially forming a "saddle-shaped" pattern (in the [Supplementary material Fig. 7a](#)). With ongoing mining, the plastic zone and tensile damage area expand vertically, reaching 160 by 300 m mined. The [Supplementary material Fig. 7b](#) illustrates the sequential damage along the  $Y=270$  cross-section, transitioning from a "saddle" to an elongated "boat-shaped" form, ultimately reaching the weathered bedrock at a stable height of 176 m, with a caving zone of 36 m. Similarly, the [Supplementary material Fig. 7c](#) shows the bottom-to-top damage progression at the mining cut along the  $X=170$  cross-section (cross-section b in the [Supplementary material Fig. 7a](#)).

[Fig. 10](#) details the dynamic evolution of overburden permeability during mining, with [Fig. 10a](#) and b focusing specifically on the changes in vertical permeability coefficients along the  $Y=270$  and  $X=170$  cross-sections, respectively. The analysis indicates that the

**Table 2**

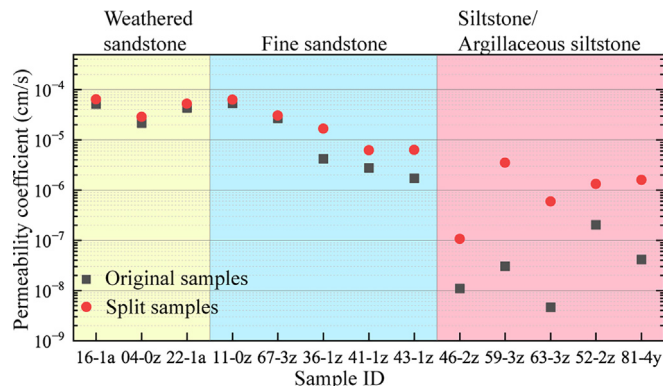
Core sample test results.

ID	Lithology	Depth (m)	Permeability coefficient (cm/s)	Tensile strength (MPa)	Damage coefficient
16-1a	Weathered sandstone	87.70	$1.20 \times 10^{-5}$	1.861	0.10
04-0z	Weathered sandstone	106.76	$2.17 \times 10^{-5}$	0.844	0.12
22-1a	Weathered sandstone	107.13	$4.38 \times 10^{-5}$	1.656	0.09
11-0z	Fine sandstone	193.06	$5.43 \times 10^{-5}$	1.825	0.08
67-3z	Fine sandstone	200.67	$2.70 \times 10^{-5}$	2.313	0.06
36-1z	Fine sandstone	205.49	$4.20 \times 10^{-6}$	2.313	0.60
41-1z	Fine sandstone	240.00	$2.76 \times 10^{-6}$	3.023	0.36
43-1z	Fine sandstone	241.60	$1.72 \times 10^{-6}$	1.997	0.57
46-2z	Siltstone	110.75	$1.09 \times 10^{-8}$	6.122	1.67
59-3z	Siltstone	133.54	$3.06 \times 10^{-8}$	6.992	2.06
63-3z	Siltstone	154.28	$4.65 \times 10^{-9}$	8.234	2.11
52-2z	Argillaceous siltstone	189.76	$2.04 \times 10^{-7}$	2.592	0.82
81-4y	Argillaceous siltstone	242.70	$4.13 \times 10^{-8}$	4.712	1.60

**Table 3**

Water inflow of 122107 working face is calculated according to the generalized method of coal mining process.

Method	Antecedent inflow (m <sup>3</sup> /h)	Middle inflow (m <sup>3</sup> /h)	Late inflow (m <sup>3</sup> /h)	Average error (%)
Virtual well	320	250	170	68.31
Specified head	38.92	141.31	187.83	68.93
Drain	207.32	342.55	316.64	32.52
CMD	137.42	341.06	898.96	11.08
Actual inflow	156	318	788	

**Fig. 8.** Permeability comparison of different lithology samples before and after splitting.

areas of high influence on vertical permeability coefficients can be divided into two main parts. The first part is located within the first 15 m above the coal seam roof, where the overburden undergoes rapid and increasing damage as mining activities progress. Notably, the permeability enhancement near the mining cut is significantly greater than that near the retreat line. The second part is situated within 50 m above the coal seam roof, where its impact becomes evident in the mid-stage of mining as the roof collapses. As mining progresses, the influence area gradually expands. Compared to the first part, the second part exhibits a smaller horizontal coverage length but a more significant influence height in the vertical direction.

Furthermore, Fig. 11 offers a more comprehensive perspective by contrasting the variation characteristics of vertical permeability coefficients at different spatial locations throughout the entire mining cycle. In the Y-direction, two locations are selected for comparison: the edge of the working face (Y=280 m) represented by the black line and the middle of the working face (Y=220 m) represented by the red line. In the Z-direction, three different levels are chosen: 15, 40, and 90 m above the coal seam, respectively. The X-direction represents the mining direction, with four

representative locations selected at 0, 60, 150, and 270 m from the mining cut, identified as a, b, c, and d, respectively.

Analysis of Fig. 11a shows that the locations 15, 40, and 90 m above the cut experience plastic damage after advancing 30, 50, and 130 m of mining, respectively. Notably, the edge of the working face continues to experience tensile effects after plastic damage, leading to a sustained increase in permeability, while the interior of the working face is primarily influenced by compaction, resulting in a gradual decrease in permeability. Fig. 11b reveals that in the horizontal direction, significant changes in the vertical permeability coefficient at monitoring points occur even 20 m before mining commences. Comparing parts b and c in Fig. 11, vertically, the first abrupt changes occur almost simultaneously at 15 and 40 m above the coal seam. Subsequently, permeability decreases due to reduced compaction until mining reaches the monitoring point, at which point a second surge in permeability occurs at 15 m above the coal seam. The second surge at 40 m above the coal seam lags behind and the lag time shortens as the distance from the cut increases. The time of permeability surge occurs slightly earlier at the edge of the working face compared to the middle, but the final increase in permeability is greater in the middle. Comparing Fig. 11d, it can be observed that the level 90 m above the coal seam is only affected by the first permeability surge. The times of these surges occur at 130, 90, 0 m after mining commences, and 30 m before mining, respectively.

#### 4.3. Regional seepage process

By organizing the variation patterns of data from various mechanical monitoring points, parameter zoning for permeability changes is conducted. By reading the permeability param of each grid within the zones and applying a formula, the equivalent hydraulic conductivity of each zone is calculated. Consequently, the permeability variation curves for each zone throughout the entire mining process are obtained. By aligning the mining process with stress periods, changes in mine water inrush throughout the mining process are derived.

Given that the horizontal disturbance range of mining activities generally coincides with the mining area, and the horizontal per-

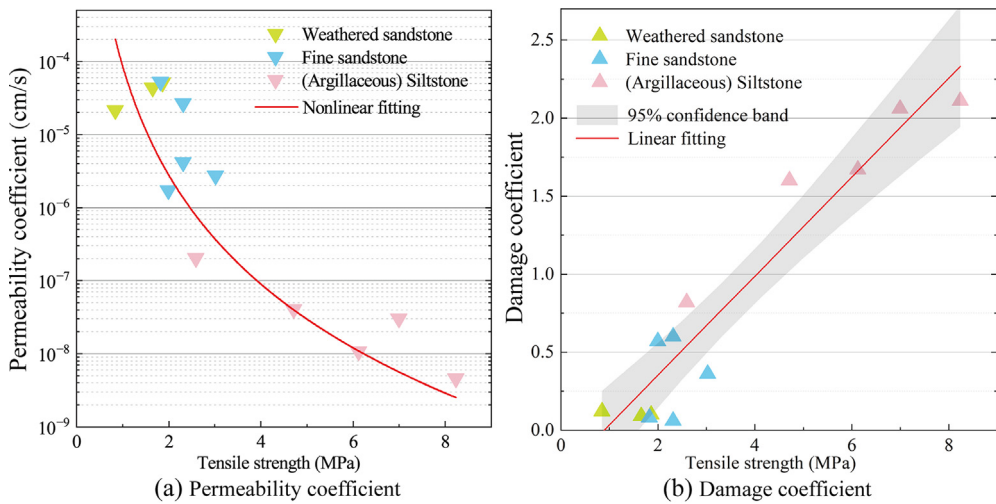


Fig. 9. Correlation between rock tensile strength and permeability.

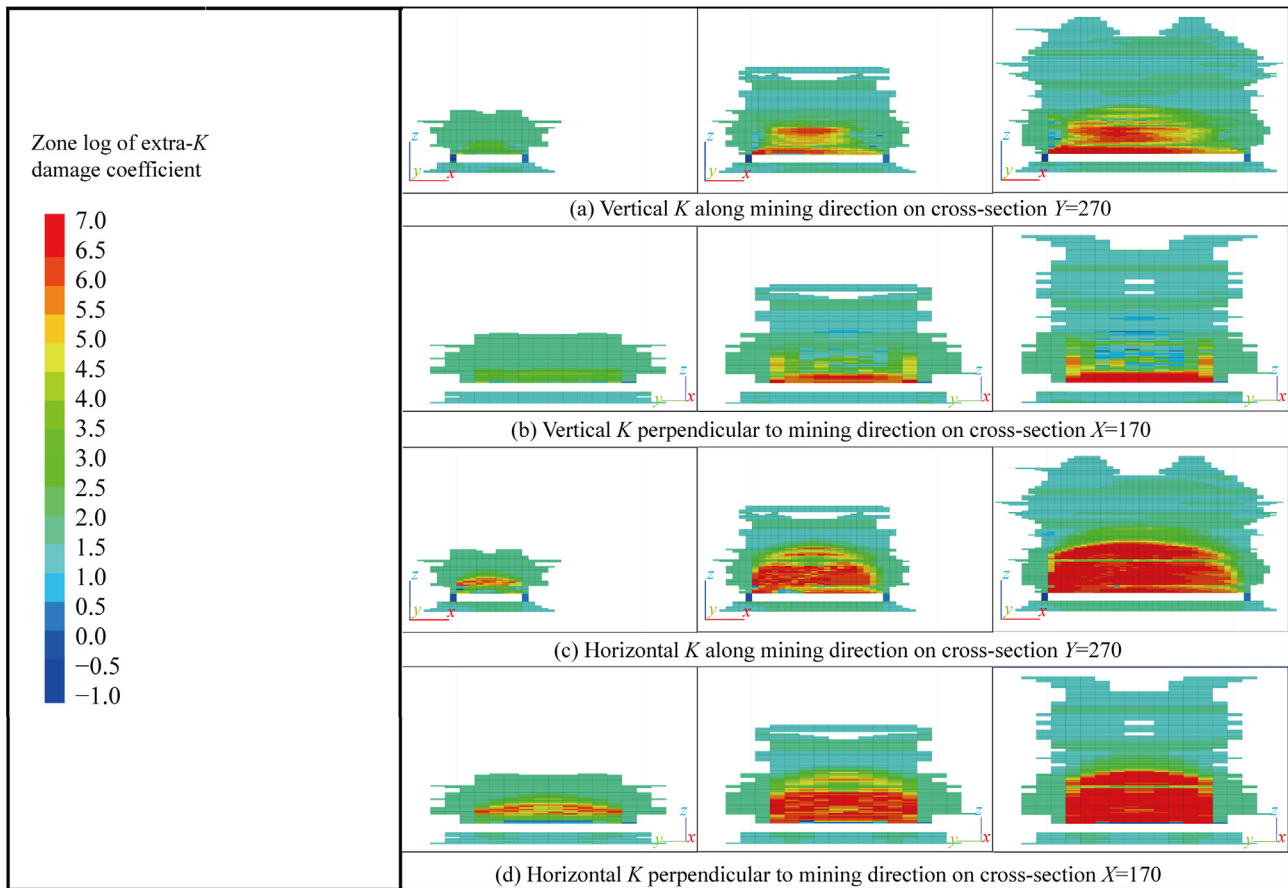
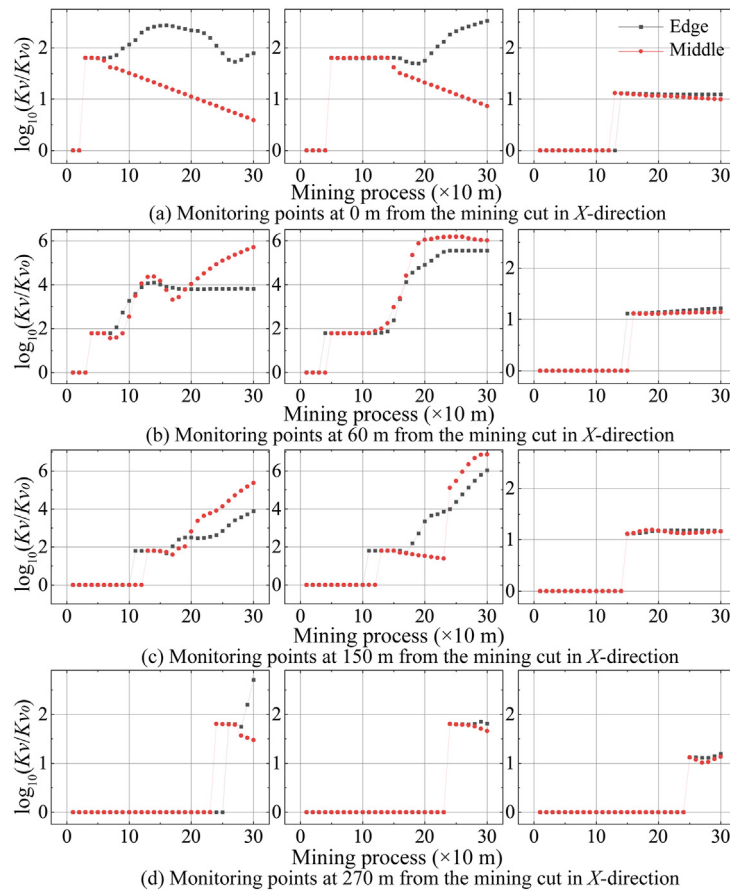


Fig. 10. Evolution of permeability during mining.

meability of normal bedrock sections is poor, with limited capacity to receive external recharge, the groundwater level variations in normal bedrock aquifers exhibit specific patterns during mining. As shown in the Supplementary material Fig. 8a, under steady-state flow conditions, a steep depression cone forms near the 09 working face. As mining progresses through different stages (Stage 1, Stage 5, Stage 10), the groundwater level in the bedrock aquifer rapidly declines, reaching near the coal seam roof within approxi-

mately 15 d. The influence range of this groundwater level depression cone aligns well with the region of permeability changes in the underlying strata induced by coal mining activities.

As illustrated in Fig. 12, a significant groundwater level drawdown funnel forms in the mining area, yet its influence radius is extremely narrow. Specifically, the groundwater level remains stable just 10 m away from the mining face. In practice, due to safety concerns, groundwater level monitoring boreholes are typi-



**Fig. 11.** Comparative analysis of permeability variation with mining progress at the middle and edge of the working face.

cally positioned far from the mining area, making it impossible to install boreholes directly above the mining face. Consequently, despite the existence of several hydrological monitoring boreholes within the bedrock aquifer, their groundwater levels remain constant throughout the mining process. Therefore, the interpolated flow field derived from the actual monitoring data also exhibits no change.

In contrast, the weathered bedrock aquifer, with its strong horizontal recharge capability, experiences a more extensive range of groundwater level influence due to coal mining disturbances. By comparing the flow field interpolated from monitoring well groundwater levels with the simulated flow field (Fig. 12), it can be observed that both maintain a high degree of consistency in terms of morphology and variation trends. Under steady-state flow conditions, a stable depression cone forms in the middle of the 09 working face, but the center of the depression cone in the simulated flow field is slightly offset towards the directly above area of the working face. This deviation is primarily attributed to the lack of direct groundwater level monitoring data directly above the working face. As mining progresses (from Stage 5 to Stage 10), the depression cone located above the 09 working face remains stable, while the depression cone above the 07 working face gradually emerges and expands, accompanied by an increase in its depth. This indicates that coal mining activities significantly impact the hydrogeological conditions even far from the direct mining area.

To further validate the accuracy of the model, a comparative analysis was conducted on groundwater level monitoring data from multiple weathered bedrock and Quaternary aquifers (in the [Supplementary material Fig. 9](#)). The results revealed that the

groundwater level trends were generally consistent, exhibiting a natural decay process. However, under the influence of mining, the amplitude of groundwater level decline significantly increased, and the goodness-of-fit ( $R^2$ ) between model predictions and measured data was greater than 0.9, indicating a high level of model reliability.

In the parameter sensitivity analysis, various parameters including horizontal permeability coefficients (HK), vertical permeability coefficients (VK), storage coefficients (SSR), and rainfall infiltration coefficients (RCH) were compared across aquifers such as rainfall, Quaternary, weathered bedrock, and bedrock (in the [Supplementary material Fig. 10](#)). The findings indicated that the vertical permeability coefficient (VK4) of the bedrock aquifer had the most significant impact on model outputs, underscoring the importance of model parameter optimization and adjustment.

Based on the identified and calibrated model parameters, a water balance calculation and prediction of mine water inflows were conducted. As shown in Fig. 13, the improved model can accurately reflect the dynamic variation characteristics of water inflows with mining progress, demonstrating a high degree of agreement with measured data. Specifically, the water inflow at the 09 working face remained relatively stable during the mining process, while the water inflow at the 07 working face increased significantly in the later stages of mining, accompanied by a decrease in the water inflow at the 09 working face. Model predictions indicate that the maximum water inflow at the 07 working face can reach  $1100 \text{ m}^3/\text{h}$ , with this peak occurring at a distance of 3400 m from the cutting eye. Through water balance analysis, it was determined that the water inflow at the 122109 working face primarily originated from the bedrock aquifer

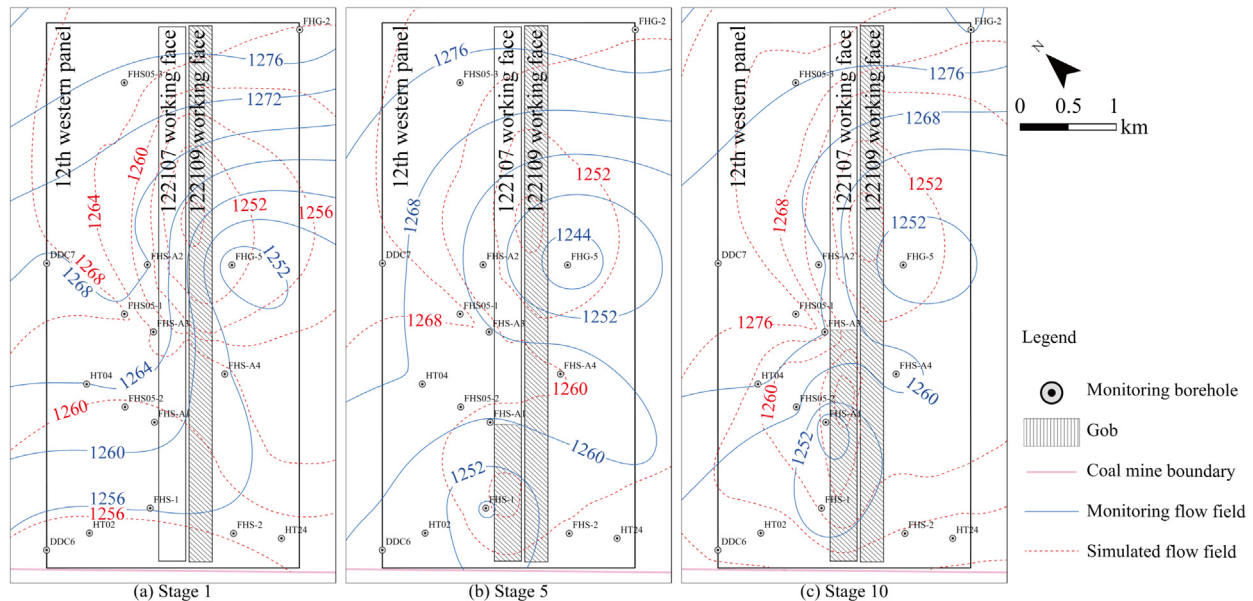


**Fig. 12.** Flow field in the weathered bedrock aquifer.

(63.01%), weathered bedrock aquifer (35.95%), and Quaternary aquifer (1.02%). In contrast, the proportions of water inflow sources at the 122,107 working face varied with mining stages, with the initial stages seeing contributions from the bedrock aquifer (25.95%), weathered bedrock aquifer (34.21%), and Quaternary aquifer (39.84%), transitioning to the later stages where the proportions were bedrock aquifer (37.49%), weathered bedrock aquifer (49.87%), and Quaternary aquifer (12.64%).

## 5. Discussion

### 5.1. Comparison with traditional mechanical simulation

Moreover, in current research, to simulate the changes in the seepage field during the mining process, a commonly employed simplified method is to set the pore pressure of mined-out elements to zero. This approach, based on hydraulic gradients, is used to simulate mine water inrush and has been widely applied in the simulation of water hazards in coal seam floors [30]. However, the occurrence mechanism of roof damage differs substantially from this. Roof water hazards arise when the water-conducting fracture zone reaches the water-rich aquifer above the coal seam [31]. Given

that the water-richness of Jurassic coal seams is relatively weak, mine water inrush primarily originates from overlying aquifers that are not directly hydraulically connected to the coal seam. Consequently, the method of setting the pore water pressure of mined-out elements to zero is no longer applicable. Instead, the newly developed mining-induced damage module based on dynamic adaptive param in this study dynamically adjusts the permeability coefficient according to the magnitude of strain during mining, thereby altering the state of the seepage field. Ultimately, through coupled analysis, the damage state of the overburden can be accurately determined.

As shown in the [Supplementary material Fig. 11](#), when there is no direct hydraulic connection between coal seams and water-bearing aquifers, traditional simulation approaches often fail to capture the true impact of mining activities on pore water pressure distribution, resulting in a post-mining pore water pressure distribution that is nearly identical to the initial state, unable to truthfully reflect the occurrence and development of water inrush phenomena. In contrast, the present simulation technology introduces a dynamic simulation mechanism for permeability changes, enabling it to accurately capture subtle variations in pore water pressure during mining. This technology not only considers the stress redistribution

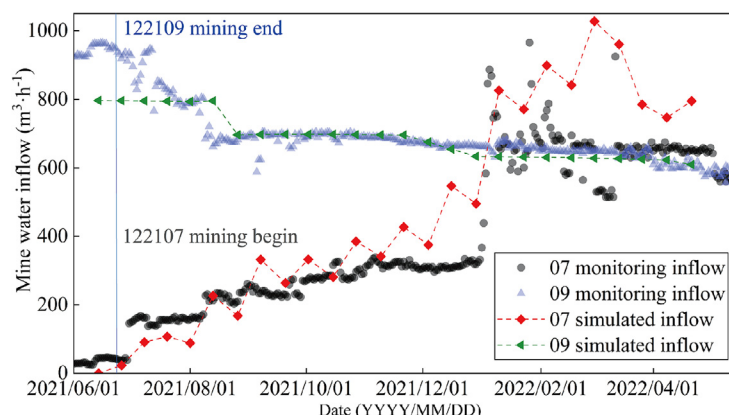


**Fig. 13.** Comparison of monitoring and simulated working face water inflow.

effects of coal seam mining on surrounding rock masses but also reflects these stress changes on groundwater flow paths and velocities through adjustments to permeability param.

Moreover, the groundwater levels computed by the flow model are input into the mechanical model for data assimilation. This iterative process continues until the outcomes from both the mechanical and hydrodynamic models converge, thereby ensuring the high precision and reliability of the simulation results. This two-way feedback mechanism not only elevates the simulation accuracy but also reinforces the models' adaptability to intricate geological conditions and hydrological processes.

### 5.2. Comparison with traditional mine water inflow prediction

Addressing the limitations of flow models in studying dynamic water inrush during coal seam mining, this innovative simulation technology achieves precise modeling of water inrush processes under complex geological conditions by assigning varying permeability characteristics across different mining stages to each overburden rock zone. In reality, traditional water flow simulation techniques primarily rely on water flow equations derived from the principle of mass conservation, which exclude stress-strain considerations. These methods exhibit significant shortcomings when tackling dynamic water inrush issues induced by coal seam mining. They often simulate mining effects in a highly generalized manner, such as through virtual well methods [32], specified head methods [33], and drainage methods [34], which presuppose the aquifer groundwater levels post-mining disturbance and drive groundwater changes through hydraulic head differences. However, these methods overlook the intricate influences of stress-strain in overburden rocks on permeability and groundwater flow paths during mining, making it difficult to accurately reflect actual water inrush processes. In contrast, the present simulation technology simulates water inrush by altering the structural state of aquifers post-mining disturbance and increasing the amount of inter-aquifer flow, which aligns more closely with actual conditions following mining disturbances.

In this case study, the actual source of mine water inrush originates from the weathered bedrock aquifer and Quaternary aquifer above the bedrock aquifer. As traditional methods cannot simulate the complex hydraulic connections between multiple aquifers under mining influence, their calculated water inrush volumes often solely derive from the bedrock aquifer, leading to underestimated results. In contrast, this innovative simulation technology accurately captures the inter-aquifer flow phenomenon between these multiple aquifers, thereby enhancing the accuracy of water inrush volume calculations. As demonstrated in [Table 3](#), the computational precision of the new technology exceeds that of traditional methods by 57%, underscoring its superiority in dynamic water inrush research.

### 5.3. Applicability and limitations of new modelling techniques

This technology is primarily applied to simulate and analyze regional groundwater flow models under mining activities, aiming to address the impact of significant geological structural changes caused by coal mining on the groundwater flow field. Its core lies in establishing a reasonable constitutive relationship for permeability evolution and revealing the laws governing overburden damage, permeability evolution, and groundwater flow field changes during mining through engineering-scale simulations. Simply put, this technology provides an effective solution for engineering simulations where water flow becomes more complex during mining activities.

In recent years, the intensification of coal mining has increasingly significantly impacted groundwater systems in large coal bases [35]. Traditional mechanical studies have primarily concentrated on overburden damage caused by mining, neglecting the broader alterations in groundwater systems. Furthermore, numerous studies on permeability changes have been conducted within the framework of previous mechanical simulations [36,37]. These studies have provided a more detailed portrayal of the rock damage process, which offers valuable insights for refining the mechanical models in this research [38,39]. However, they have emphasized the impact of pore pressure changes on rock damage more, with less attention devoted to water exchange and migration issues. Consequently, this has hindered a deeper understanding of mine water hazards and ecological and environmental problems.

In the research conducted at Caojiatan Coal Mine, high-intensity mining activities led to groundwater outside the overburden damage zone contributing to mine inflow, including lateral recharge from weathered bedrock aquifers and vertical recharge from Quaternary aquifers. As evident from [Fig. 12](#), bedrock aquifers exhibit low permeability with limited influence scopes (confined to mining areas), while weathered bedrock aquifers display high permeability with widespread impacts (affecting areas several times larger than the mining area). The Quaternary aquifer, located above the water-conducting fractured zone caused by mining, experiences leakage due to increased hydraulic gradients between upper and lower aquifers induced by mining. Therefore, mechanical studies confined solely to the mining-induced damage zone are insufficient to address water hazards and ecological issues in western mining areas. The modular simulation technology proposed in this paper aims to further refine the groundwater flow model based on mechanical research, fully capturing the entire process of groundwater changes in mines during mining activities. This technology provides effective support for safe mining and the protection of ecological groundwater resources, possessing significant practical significance and potential value.

In the current study, to ensure smooth data transfer and effective coupling processes, the mechanical damage process was simplified to a certain extent, and the FLAC model, which utilizes the finite difference method similar to the flow model, was selected. This choice was based on the FLAC model's better consistency with the flow model in terms of numerical methods and data structures, thereby facilitating the coupled simulation. Despite undergoing necessary simplifications as an auxiliary tool for the flow model, the mechanical model will undergo further refinement in subsequent research, with a focus on deepening the investigation of the interaction mechanism between complex water flow processes and mechanical damages.

## 6. Conclusions

The complex interplay between the mechanical property variations in rock strata and fracture seepage during coal mining is a pivotal factor constraining the safe production of mines and the protection of mine ecological water resources. To precisely characterize this dynamic process, the present study, grounded on an in-depth analysis of the integration challenges in mechanical and flow field simulations, innovatively proposes a simulation technology encompassing the entire mining process. This technology, through the construction of a modular simulation framework, not only achieves a comprehensive portrayal of the stress-strain-fracture-permeability characteristics of the overburden rocks during mining but also successfully feeds back the results of mechanical damage simulations dynamically into the groundwater system, thereby driving the precise evolution of

the flow field. The following are the key conclusions drawn from this study:

- (1) A mathematical model for the permeability evolution throughout the entire stress-strain process of rocks was established through theoretical derivation and experimental validation. By introducing a damage coefficient, the process of permeability mutation is described. Based on experimental results, a linear relationship between the  $\alpha$  and  $T$ , in MPa, was established:  $\alpha = -0.282 + 0.317T$ .
- (2) Based on the “two-stage, cross-scale constitutive model”, the spatio-temporal evolution of overburden permeability throughout the entire coal mining process was investigated. After plastic damage, the overburden rocks at the edges of the working face experience continuous tensile effects, leading to an increase in permeability. Horizontally, a notable enhancement in overburden permeability is first observed approximately 40 m before mining commences, with a further abrupt increase when mining reaches the overburden. Vertically, the overburden within 15 m above the coal seam roof rapidly deteriorates with mining activities, while the deterioration of the overlying strata exhibits hysteresis, with the lag time decreasing as the distance from the cut-off increases.
- (3) Leveraging an explicit coupling simulation strategy, a modular simulation technology for the entire mining process in mines was developed. Through coupled mechanical and flow field analysis, the permeability zones of the overburden are dynamically adjusted, enabling precise simulations of the complex hydraulic connections between multiple aquifers and dynamic water inrush processes during coal mining. Consequently, the accuracy of water inrush volume calculations was improved by 57%.

## Acknowledgments

This work was supported by the National Natural Science Foundation of China (Nos. 42027801, 42072284, and 42372297), the National Key Research and Development Program of China (Nos. 2023YFC3012102 and 2021YFC2902004), and the Fundamental Research Funds for the Central Universities (No. 2023ZKPYSH01).

## Supplementary data

Supplementary data to this article can be found online at <https://doi.org/10.1016/j.ijmst.2024.11.014>.

## References

- [1] Liu XX, Zeng YF, Wu Q, Meng SH, Liang JY, Hou ZP. Ecological-based mining: A coal-water-thermal collaborative paradigm in ecologically fragile areas in Western China. *Engineering* 2024;38:209–22.
- [2] Li CC, Gao XB, Xiang XL, Jiang CF, Duan Y, Wang WZ, Zhang X, Tan T, Wang QR, Wang YX. Intense human activities induce the dynamic changes of interaction pattern between Karst water-quaternary groundwater in the basin-mountain coupling belt over the past 60 Years. *Water Resour Res* 2024;60(2):e2023wr035211.
- [3] Zeng YF, Meng SH, Wu Q, Mei AS, Bu WY. Ecological water security impact of large coal base development and its protection. *J Hydrol* 2023;619:129319.
- [4] Wu Q, Liu YZ, Zhou WF, Li BY, Zhao B, Liu SQ, Sun WJ, Zeng YF. Evaluation of water inrush vulnerability from aquifers overlying coal seams in the menkeqing coal mine. *China Mine Water Environ* 2015;34(3):258–69.
- [5] China Energy Big Data Report. Beijing: China energy media Institute for energy security new strategy research; 2024.
- [6] Zeng YF, Pang ZZ, Wu Q, Hua ZL, Lv Y, Wang L, Zhang Y, Du X, Liu SQ. Study of water-controlled and environmentally friendly coal mining models in an ecologically fragile area of Northwest China. *Mine Water Environ* 2022;41(3):802–16.
- [7] Mei AS, Wu Q, Zeng YF, Cui YS, Zhao D. Evaluation of water inrush vulnerability and feasibility analysis of mining under rivers: A case study involving the Jinjie coal mine in China. *Mine Water Environ* 2023;42(2):312–29.
- [8] Wang GF, Xu YX, Ren HW. Intelligent and ecological coal mining as well as clean utilization technology in China: Review and prospects. *Int J Min Sci Technol* 2019;29(2):161–9.
- [9] Hua ZL, Zhang Y, Meng SH, Wang L, Wang XJ, Lv Y, Li JM, Ren SF, Bao H, Zhang ZH, Zhao LE, Zeng YF. Response characteristics and water inflow prediction of complex groundwater systems under high-intensity coal seam mining conditions. *Water* 2023;15(19):3376.
- [10] Zhang S, Liu XL. A semi-analytical solution for the equivalent permeability coefficient of the multilayered porous medium with continuous fracture. *Water Resour Res* 2024;60(2):e2023WR036203.
- [11] Vora A, Cai XM, Chen YN, Li DH. Coupling reservoir operation and rainfall-runoff processes for streamflow simulation in watersheds. *Water Resour Res* 2024;60(6):e2023WR035703.
- [12] Soulaine C. Micro-continuum modeling: An hybrid-scale approach for solving coupled processes in porous media. *Water Resour Res* 2024;60(2):e2023WR035908.
- [13] Li H, Wang FG, Wang YH, Yuan YL, Feng GH, Tian HL, Xu TF. Phase-field modeling of coupled reactive transport and pore structure evolution due to mineral dissolution in porous media. *J Hydrol* 2023;619:129363.
- [14] Markstrom SL, Niswonger RG, Regan RS, Prudic DE, Barlow PM. GSFLOW – coupled ground-water and surface-water flow model based on the integration of the precipitation-runoff modeling system (PRMS) and the modular ground-water flow model (MODFLOW-2005). U.S. Geol Surv Tech Meth 2008;6:D1.
- [15] Pollock DW. User's guide for MODPATH/MODPATH-PLOT, Version 3; A particle tracking post-processing package for MODFLOW, the U.S. Geological Survey finite-difference ground-water flow mode. US Geol Surv Tech Meth 1994;94–464.
- [16] Zheng C, Hill MC, Cao G, Ma R. MT3DMS: Model use, calibration, and validation. *Trans TASABE* 2012;55(4):1549–59.
- [17] Langevin CD, Thorne DT, Dausman AM, Sukop MC, Guo W. SEAWAT Version 4—A computer program for simulation of multi-species solute and heat transport. *US Geol Surv Tech Meth* 2008;6:A22.
- [18] Leake S, Galloway D. MODFLOW Ground-Water Model – User Guide to the Subsidence and Aquifer-System Compaction Package (SUB-WT) for Water-Table Aquifers. US Geol Surv Tech Meth 2007;6:A23.
- [19] Zhao YL, Liu Q, Zhang CS, Liao J, Lin H, Wang YX. Coupled seepage-damage effect in fractured rock masses: model development and a case study. *Int J Rock Mech Min Sci* 2021;144:104822.
- [20] Wu Q, Dong DL, Wu G, Liu JT. Visualized professional software (visual MODFLOW) for water resources evaluation and its application potential. *Hydrogeol Eng Geol* 1999;05:23–5. In Chinese.
- [21] Wunsch A, Liesch T, Broda S. Deep learning shows declining groundwater levels in Germany until 2100 due to climate change. *Nat Commun* 2022;13(1):1221.
- [22] Wang CL, Zhao Y, Ning L, Bi J. Permeability evolution of coal subjected to triaxial compression based on *in situ* nuclear magnetic resonance. *Int J Rock Mech Min Sci* 2022;159:105213.
- [23] Cai JC, Wei W, Hu XY, Liu RC, Wang JJ. Fractal characterization of dynamic fracture network extension in porous media. *Fractals* 2017;25(2):1750023.
- [24] Zhao Y, Bi J, Wang CL, Liu PF. Effect of unloading rate on the mechanical behavior and fracture characteristics of sandstones under complex triaxial stress conditions. *Rock Mech Rock Eng* 2021;54(9):4851–66.
- [25] Meng ZP, Shi XC, Li GQ. Deformation, failure and permeability of coal-bearing strata during longwall mining. *Eng Geol* 2016;208:69–80.
- [26] Rutqvist J. Status of the TOUGH-FLAC simulator and recent applications related to coupled fluid flow and crustal deformations. *Comput Geosci* 2011;37(6):739–50.
- [27] Langevin CD, Hughes JD, Provost AM, Banta ER, Niswonger RG, Panday S, Provost AM. Documentation for the MODFLOW 6 Groundwater Flow (GWF) Model US Geol Surv Tech Meth 2017;6:A55.
- [28] Niswonger RG, Panday S, Ibaraki M. MODFLOW-NWT, A Newton formulation for MODFLOW-2005. U.S. Geol Surv Tech Meth 2011;6:A37.
- [29] McDonald MG, Harbaugh AW. A modular three-dimensional finite-difference ground-water flow model. *Tech Water-Resour Invest US Geol Surv* 1988;06-A1.
- [30] Li HL, Bai HB. Simulation research on the mechanism of water inrush from fractured floor under the dynamic load induced by roof caving: Taking the Xinji second coal mine as an example. *Arab J Geosci* 2019;12(15):466.
- [31] Zeng YF, Wu Q, Liu SQ, Zhai YL, Lian HQ, Zhang W. Evaluation of a coal seam roof water inrush: Case study in the wangjialing coal mine. *China Mine Water Environ* 2018;37(1):174–84.
- [32] Zhai HT, Wang JC, Li YC, Rao ZX, He K, Hao SY, Huo AD, Adnan A. Prediction of the mine water inflow of coal-bearing rock series based on well group pumping. *Water* 2023;15(20):3680.
- [33] Zhao CH, Wang SD, Jin DW, Zhang PY, Zhu KP, Ji ZK, Xu F. Research status and evaluation methods on the impact of coal mining on groundwater resources in Shaanbei and Shendong coal bases. *J Green Mine* 2024;2(2):150–9. In Chinese.
- [34] Peksezer-Sayit A, Cankara-Kadioglu C, Yazicigil H. Assessment of dewatering requirements and their anticipated effects on groundwater resources: A case study from the caldag nickel mine, western Turkey. *Mine Water Environ* 2015;34(2):122–35.
- [35] Meng SH, Wu Q, Zeng YF, Mei AS, Yang GQ, Hua ZL, Yang L, Zhang Y. Evaluating the impact of coal seam roof groundwater using variable weights theory: A

- special emphasis on skylight-type water inrush pattern. *J Hydrol Reg Stud* 2024;56:102009.
- [36] Wang K, Tang CN, Li G, Zhang HH. Numerical simulation of spatial crack growth and the local failure process of rock using the SMDSM empowered by structured 3-D hierarchical meshes. *Rock Mech Rock Eng* 2024;57(9):6951–69.
- [37] Liu XR, Li PY, Guo XY, Luo XY, Zhou XH, Miao LL. A statistical damage-based constitutive model for shearing of rock joints in brittle drop mode. *Int J Min Sci Technol* 2024;34(8):1041–58.
- [38] Xia YJ, Yao MY, Li TJ, Yang H, Tang CA. Numerical analysis of hydraulic fracture propagation in deep shale reservoir with different injection strategies. *J Rock Mech Geotech Eng* 2024;16(9):3558–74.
- [39] Yu QJ, Du SG, Zhu QZ, Luo ZY, Liu SL, Zhao LY. An extended micromechanical-based plastic damage model for understanding water effects on quasi-brittle rocks. *Int J Min Sci Technol* 2024;34(3):289–304.